Smooth Local Correlation-based Transition Model for the Spalart-Allmaras Turbulence Model

Michael G. H. Piotrowski*

NASA Ames Research Center, Moffett Field, CA 94035
Institute for Aerospace Studies, University of Toronto, ON M3H 5T6

David W. Zingg[†]

Institute for Aerospace Studies, University of Toronto, ON M3H 5T6

A smooth version of the γ-$\tilde{Re}_{\theta t}$ local correlation-based transition model (LM2015) for the Spalart-Allmaras (SA) turbulence model is presented. The LM2015 model with helicity-based crossflow correlations is modified and coupled to the SA turbulence model, designated SA-LM2015. The LM2015 and SA-LM2015 transition models include source terms that contain stiff and non-smooth functions. Approximations to these functions are introduced to eliminate discontinuities and improve the numerical behaviour of the model, with the smooth model designated SA-sLM2015. Deep convergence is achieved using a fully-coupled, implicit Newton-Krylov algorithm globalized using an efficient pseudo-transient continuation strategy. Modifications to the Newton-Krylov algorithm are introduced, including a source term time stepping strategy, to address the large sources introduced by the turbulence and transition model equations. Two- and three-dimensional transition test cases demonstrate that both models, SA-LM2015 and SA-sLM2015, are able to predict transition due to a variety of mechanisms accurately, with the smooth variant displaying significantly improved numerical behaviour. Several of the strategies presented, including the smoothing techniques and source term time stepping, could be useful in the context of other transition models as well.

Nomenclature

d	minimum off-wall distance
$H_{\text{crossflow}}$	crossflow strength parameter
h	surface roughness height (rms)
M	Mach number
p	smooth maximum/minimum function parameter
p_{switch}	proximity switch cutoff value, 10^{-15}

---
*NASA Pathways Ph.D. Candidate, University of Toronto, NASA Computational Aeroscience Branch, AIAA Student Member, michael.g.piotrowski@nasa.gov, m.piotrowski@mail.utoronto.ca

[†]University of Toronto Distinguished Professor of Computational Aerodynamics and Sustainable Aviation, Associate Fellow AIAA, dwz@oddjob.utias.utoronto.ca

Re	Reynolds number
$\tilde{Re}_{\theta t}$	transported quantity of the local transition onset momentum-thickness Reynolds number
$Re_{\theta t}$	transition onset momentum-thickness Reynolds number
Re_S	strain-rate magnitude Reynolds number
Re_Ω	vorticity Reynolds number
R_T	eddy viscosity ratio
S	strain rate magnitude
Tu	turbulence intensity
$\vec{U}$	unit velocity vector
U	local velocity magnitude
u_i	Cartesian velocity component
$\vec{\Omega}$	vorticity vector
Ω	vorticity magnitude
$\Omega_{\text{streamwise}}$	streamwise vorticity, helicity
γ	intermittency
ρ	density
μ	molecular viscosity
μ_t	eddy viscosity
λ_θ	pressure gradient parameter
δ	boundary layer thickness
θ_t	transition onset momentum thickness
γ_{source}	largest positive source-term Jacobian eigenvalue
ϕ_P	smooth maximum/minimum function
ϕ_{switch}	proximity switch for the smooth maximum/minimum function

I. Introduction

Laminar-flow wing designs produce an increased laminar extent of the boundary layer, resulting in a decrease in viscous drag [1]. These drag savings have the potential to significantly reduce the fuel burn of transport aircraft, where viscous drag constitutes approximately 50% of the total drag [2]. The potential of laminar-flow designs has been demonstrated by various studies which suggest the application of laminar flow control to large commercial aircraft can reduce aerodynamic drag by approximately 10% [3].

In the near term, natural laminar flow (NLF) is being investigated for winglet, tail, and nacelle designs, with the Boeing 787-8 and 777X representing the first commercial applications of NLF nacelles to large transport aircraft, and the 737 Max aircraft exploiting laminar flow for both the nacelle and winglet designs [4]. In the future, the design of wings which exploit significant regions of laminar flow can result in more significant drag reduction. The Airbus BLADE project is investigating this, while experimental studies of the NASA common research model NLF (CRM-NFL) demonstrate that it is possible to design transport wings with high sweep and Reynolds numbers with significant regions of laminar flow [5–7]. However, there are several operational challenges that need to be addressed. For example, the Boeing 757 EcoDemonstrator is investigating the effect of anti-insect devices and surface coatings for the application of laminar flow on wing leading edge surfaces.

Efficient high-fidelity numerical optimization algorithms provide the designers of next generation aircraft with powerful tools for the development of more fuel-efficient designs [8–10]. The integration of a flow solver with transition prediction capability into an aerodynamic shape optimization algorithm will allow for the study of various trade-offs in the design of novel NLF wing configurations. The design of aircraft configurations using design tools capable of incorporating and exploiting NLF, which requires the ability to predict laminar-turbulent transition efficiently, could play a key role in reducing the environmental impact of aviation.

There are several mechanisms for boundary-layer transition. The method of transition depends on the application being studied, such as flow past wings, airframes, rotor blades, and wind turbine blades, as well as the characteristics of the flow, such as Reynolds number, angle of attack, pressure gradient, and turbulence intensity. For a swept transport-aircraft wing the dominant mechanisms for transition result from Tollmien-Schlichting wave growth leading to natural transition, crossflow instabilities resulting from highly swept wings, concave curvature producing Görtler instabilities, and attachment-line instabilities as a result of large leading edge radius and sweep at the root of the wing [11]. While the last two mechanisms can be prevented by appropriate profile design, balancing natural and crossflow-induced transition can be difficult as favourable pressure gradients used to stabilize stream-wise instabilities destabilize crossflow instabilities [11]. The effects of laminar-turbulent transition can be included in numerical simulations using various transition prediction and modeling techniques, consisting of either local or non-local operations [12–14].

Flow solvers based on the Reynolds-Averaged Navier-Stokes (RANS) equations provide an excellent balance between accuracy, robustness, and efficiency, making them a suitable choice for practical engineering applications that require the solution of large and complex geometries. However, the turbulence models typically used in RANS solvers do not have the stand-alone capability to predict boundary-layer transition. In order to predict transition, one must apply a transition criterion. Reviews by Arnal et al. [12, 13] and Pasquale and Rona [14] describe the advantages and disadvantages of several approaches for coupling transition prediction criteria into RANS solvers. The most widely implemented transition prediction strategies for practical engineering applications are based on either the e^N criterion or on transition onset functions.

The e^N method for predicting transition is a semi-empirical approach, with the N-factor depending on free-stream flow conditions, based on linear stability theory. To apply the e^N criterion one must first approximate the N-factor curves which represent the amplification ratios of the unstable frequencies of the disturbances in the boundary-layer. This can be achieved using stability analysis methods such as the linearized or Parabolized Stability Equations (PSE) [15, 16], or through the use of simplified e^N envelope methods, developed by Drela and Giles [17], and used by Rashad and Zingg [18] and Mayda [19], depending on the level of fidelity required in a simulation.

A boundary-layer code can be used to increase the accuracy in determining the boundary-layer edge, which is required to satisfy the requirements of the stability analysis [20, 21]. However, with sufficient grid resolution it is possible to define the boundary-layer edge and extract the boundary-layer properties based on the RANS solution accurately, without using a boundary-layer solver [18, 21]. The influence of the grid resolution on the stability analysis was studied in detail by Krimmelbein and Radespiel [21].

Transition models based on the e^N method are able to accurately predict natural- and separation-induced transition. In addition, correlations for crossflow instabilities (such as the C1 criterion [22]) have been successfully combined with these approaches, with experimental validation demonstrating accurate transition prediction on transonic swept wings in three dimensions [23–27]. However, e^N methods require non-local boundary-layer quantities that are not directly accessible in RANS-based CFD codes [28].

In the context of the current work, the requirement that the transition model be formulated locally is significant. Modern CFD codes utilize domain decomposition and parallel computation to increase the efficiency of simulations. Non-local operations, such as integrating quantities over the boundary-layer, introduce difficulties to this process. Of the many transition models developed for RANS-based turbulence models, two which satisfy the requirement of a fully local formulation are the empirical correlation-based γ-$\tilde{R}e_{\theta t}$ local correlation-based transition model developed by Langtry and Menter (LM2009) [29] and the Amplification Factor Transport (AFT) transition model developed by Coder and Maughmer [30, 31] and later revised by Coder [32–35].

The AFT transition model is based on the approximate envelope method for Tollmien-Schlichting wave growth, developed by Drela and Giles [17], and is able to predict natural and separation-induced transition in subsonic and transonic flow regimes. The model consists of a single transport equation for the envelope amplification factor $\tilde{n}$ with a locally-derived approximation for the boundary-layer shape factor. The transition model was originally coupled directly to the one-equation Spalart-Allmaras (SA) eddy-viscosity model [36], resulting in a two-equation coupled system [30–33]. The most recent model [34] is coupled to an additional, intermittency equation, inspired by the work of Langtry and Menter [29], resulting in a three-equation coupled system. Recent work by Xu et al. [37] extended the AFT model to include crossflow effects, using the Falkner-Skan and Cooke equations to develop correlations for local approximations of nonlocal boundary-layer quantities, with promising results. This work involved coupling the model to the SST turbulence model, resulting in a four-equation system.

The transition model formulated by Langtry and Menter [29] is composed of two transport equations. The first is an equation for the intermittency, γ, which is used to trigger the turbulence transition process by controlling the level of turbulence in the boundary layer. The second is an equation for the transition momentum-thickness Reynolds number, $\tilde{Re}_{\theta t}$, which in the free-stream is equal to the value produced by the empirical correlations, $Re_{\theta t}$, and is diffused into the boundary layer using a standard diffusion term. Of the various crossflow transition models developed for the γ-$\tilde{Re}_{\theta t}$ transition model, two maintain a fully-local formulation, methods based on the local C1 criterion [38–41] and local helicity approaches [42, 43]. The local C1 approach uses the solutions of the Falkner-Skan and Cooke equations and is therefore only expected to work for wing-like geometries with high aspect ratios [40], unlike methods based on the local helicity.

Crossflow instability correlations based on the local helicity were initially developed by Muller and Herbst [42], with more recent correlations, which include a framework for introducing roughness effects, developed by Langtry et al. (LM2015) [43]. Grabe and Krumbein [40] conducted simulations using correlations based on both the C1 and helicity approaches. The C1 approach yielded more accurate results in terms of the comparison of predicted and measured transition locations on infinite swept wing flows, while the local helicity approach produced more accurate transition locations for non wing-like geometries [40].

The local helicity-based correlations developed by Muller and Herbst [42] and Langtry et al. [43] both consist of an additional source term in the $\tilde{Re}_{\theta t}$ equation that acts as a sink to reduce the value of $\tilde{Re}_{\theta t}$ in regions of significant crossflow, triggering transition further upstream. While the crossflow correlations of Muller and Herbst [42] and Langtry et al. [43] are similar, the latter represents a more thoroughly validated model [44]. Furthermore, the ability of the Langtry model to include roughness effects expands the applicability of the model.

The original γ-$\tilde{Re}_{\theta t}$ LM2009 model developed by Langtry and Menter [29] was coupled with the two-equation SST turbulence model [45]. Subsequent extensions of this model to include crossflow instabilities with correlations based on the local helicity by Grabe and Krumbein [40], Muller and Herbst [42], and Langtry et al. [43] also included this coupling, while Nie et al. [46] investigated the performance of the Langtry-Menter model with C1 and helicity-based crossflow correlations coupled with a Reynolds stress model.

Medida and Baeder [47] modified the γ-$\tilde{Re}_{\theta t}$ model to be compatible with the SA turbulence model, and developed a new set of correlations validated using several test cases, designating this model the γ-$\tilde{Re}_{\theta t}$-SA transition model. Recent work demonstrated the γ-$\tilde{Re}_{\theta t}$-SA model coupled with the crossflow correlations developed by Muller and Herbst [42] was able to predict transition for several three-dimensional test cases, including a swept wing, requiring only a slight modification [48]. However, their current formulation contains a function, G_{onset}, which requires non-local flow information. More recently, Carnes and Coder [49] successfully coupled the algebraic helicity-based crossflow correlations developed by Langtry et al. [43] to the AFT model, with the results comparing well to experiment.

The goal of this work is to develop a RANS-based Newton-Krylov flow solver with laminar-turbulent boundary-layer

transition prediction capabilities, to be used in a high-fidelity discrete-adjoint gradient-based aerodynamic shape optimization algorithm. To achieve this goal, the γ-$\tilde{R}e_{\theta t}$ LM2015 transition model with helicity-based crossflow correlations [43] is modified and coupled to the one-equation SA turbulence model, while maintaining a fully-local formulation, reducing the computational cost of the original four-equation system (Section II). This model will be referred to as the SA-LM2015 transition model. Smooth approximations of non-differentiable functions are developed to eliminate discontinuities in the model. Additionally, modifications to numerically stiff functions are produced in order to improve numerical convergence. This new, smooth model is designated the SA-sLM2015 transition model (Section III). Numerical methods for addressing the strong source terms present in the SA-LM2015 and SA-sLM2015 models, including a source term time stepping strategy, are developed, and their implementation in the Newton-Krylov framework is discussed (Section IV). A range of two- and three-dimensional transition test cases are simulated, with the results demonstrating that the SA-LM2015 and SA-sLM2015 transition models are able to accurately predict transition due to a variety of transition mechanisms, with the SA-sLM2015 model demonstrating significantly improved convergence characteristics (Section V).

II. SA-LM2015 Transition Model

The γ-$\tilde{R}e_{\theta t}$ LM2015 model with helicity-based crossflow correlations [43] is modified and coupled to the SA turbulence model [36]. The LM2015 model is decoupled from the SST turbulence model using modifications to the R_T and F_{wake} functions. Schücker [50] suggests replacing the specific turbulence dissipation rate, ω, in the original F_{wake} function with velocity gradients. This approach is adopted in the current work using the strain-rate magnitude. A simplification of the $F_{\theta t}$ function is introduced, which reduces the amount of non-smooth minimum/maximum operators present in the model. An adjustment to the F_{onset1} term was applied to recalibrate the model, and the strain-rate magnitude in the original intermittency production term is replaced by vorticity magnitude to make the model more stable near laminar separation bubbles. The separation-induced transition modification developed by Langtry [51] was neglected, as the delay in the growth of turbulence after laminar separation bubbles produced by the SST turbulence model is not reproduced by the SA turbulence model, which is demonstrated by the results in Section V.

The remaining terms and coefficients remain unchanged from the original model. The modified LM2015 model with helicity-based crossflow correlations coupled to the SA turbulence model, designated SA-LM2015, is presented as follows.

A. Momentum-thickness Reynolds number transport equation

The transport equation for the momentum-thickness Reynolds number, non-dimensionalized by freestream quantities and written in non-conservative form to be consistent with the SA turbulence model, is defined as:

$$\frac{\partial \tilde{Re}_{\theta t}}{\partial t} + u_j \frac{\partial \tilde{Re}_{\theta t}}{\partial x_j} = P_{\theta t} + D_{\text{scf}} + \frac{1}{Re}\frac{\partial}{\partial x_j}\left[\sigma_{\theta t}(\nu + \nu_t)\frac{\partial \tilde{Re}_{\theta t}}{\partial x_j}\right], \tag{1}$$

$$P_{\theta t} = \frac{c_{\theta t}}{t}(Re_{\theta t} - \tilde{Re}_{\theta t})(1 - F_{\theta t}), \tag{2}$$

$$F_{\theta t} = F_{\text{wake}}e^{-(\frac{d}{\delta})^4}, \tag{3}$$

$$\delta = \frac{50d\Omega}{U}\delta_{BL}; \quad \delta_{BL} = \frac{15}{2}\theta_{BL}; \quad \theta_{BL} = \frac{\tilde{Re}_{\theta t}\mu}{\rho U}\frac{1}{Re}, \tag{4}$$

$$F_{\text{wake}} = e^{\frac{-Re_S}{1E+6}}; \quad Re_S = \frac{\rho d^2 S}{\mu}Re, \tag{5}$$

$$c_{\theta t} = 0.03; \quad \sigma_{\theta t} = 2.0, \tag{6}$$

$$t = \frac{500\mu}{\rho U^2}\frac{1}{Re}, \tag{7}$$

where $Re = \frac{\rho_\infty a_\infty l}{\mu_\infty}$, '$a$' is the sound speed, '$l$' is the characteristic (reference) length, and '∞' denotes a freestream quantity. The non-dimensionalization procedure for the transition model equations is consistent with the procedure for the Navier-Stokes equations, which is described in [52] and is used, for example, in the well-known OVERFLOW flow solver[*]. For the cases presented in the current work the reference length is specified as the root chord. The natural and bypass transition empirical correlations are defined as follows:

$$Re_{\theta t} = \frac{\rho U \theta}{\mu}Re = \begin{cases} \left[1173.51 - 589.428Tu + \frac{0.2196}{Tu^2}\right]F(\lambda_\theta) & Tu \le 1.3, \\ 331.50[Tu - 0.5658]^{-0.671}F(\lambda_\theta) & Tu > 1.3, \end{cases} \tag{8}$$

$$F(\lambda_\theta) = \begin{cases} 1 - [-12.986\lambda_\theta - 123.66\lambda_\theta^2 - 405.689\lambda_\theta^3]e^{-[\frac{Tu}{1.5}]^{1.5}} & \lambda_\theta \le 0, \\ 1 + 0.275[1 - e^{[-35\lambda_\theta]}]e^{-[\frac{Tu}{0.5}]} & \lambda_\theta > 0, \end{cases} \tag{9}$$

where the local pressure gradient parameter is given by:

$$\lambda_\theta = \frac{\rho\theta^2}{\mu}\frac{dU}{ds}Re; \quad U = (u^2 + v^2 + w^2)^{\frac{1}{2}}, \tag{10}$$

$$\frac{dU}{ds} = \left[\left(\frac{u}{U}\right)\frac{dU}{dx} + \left(\frac{v}{U}\right)\frac{dU}{dy} + \left(\frac{w}{U}\right)\frac{dU}{dz}\right], \tag{11}$$

$$\frac{dU}{dx} = (u^2 + v^2 + w^2)^{-\frac{1}{2}} \cdot \left[u\frac{du}{dx} + v\frac{dv}{dx} + w\frac{dw}{dx}\right], \tag{12}$$

$$\frac{dU}{dy} = (u^2 + v^2 + w^2)^{-\frac{1}{2}} \cdot \left[u\frac{du}{dy} + v\frac{dv}{dy} + w\frac{dw}{dy}\right], \tag{13}$$

$$\frac{dU}{dz} = (u^2 + v^2 + w^2)^{-\frac{1}{2}} \cdot \left[u\frac{du}{dz} + v\frac{dv}{dz} + w\frac{dw}{dz}\right]. \tag{14}$$

The local turbulence intensity is not directly available when using the SA turbulence model. However, Suluksana et al. [53] demonstrated it can be redundant to use the local value of the turbulence intensity, Tu, as well as the pressure

---

[*]https://overflow.larc.nasa.gov/home/users-manual-for-overflow-2-2/, accessed August 2020

gradient parameter λ_θ, since the effects of pressure gradient are reduced by the decay of the local turbulence intensity. A favourable pressure gradient accelerates the flow leading to a decrease in the turbulence intensity, and therefore momentum-thickness Reynolds number, while an adverse pressure gradient leads to a reduction in turbulence intensity. The free-stream turbulence intensity value, Tu_∞, is used throughout the domain in the current work, which is consistent with the approach taken by Medida and Baeder [47].

The helicity-based stationary crossflow correlations developed by Langtry et al. are defined below [43]:

$$D_{\text{scf}} = \frac{c_{\theta t}}{t} c_{\text{crossflow}} \min(Re_{\text{scf}} - \tilde{Re}_{\theta t}, 0)(F_{\theta t}), \tag{15}$$

$$c_{\text{crossflow}} = 0.6, \tag{16}$$

$$Re_{\text{scf}} = \frac{\rho\left(\frac{U}{0.82}\right)\theta_t}{\mu} Re = -35.088 \ln\left(\frac{h}{\theta_t}\right) + 319.51 + f(\Delta H^+_{\text{crossflow}}) - f(\Delta H^-_{\text{crossflow}}), \tag{17}$$

$$\Delta H_{\text{crossflow}} = H_{\text{crossflow}}\left(1.0 + \min\left[R_T, 0.4\right]\right); \quad R_T = \frac{\mu_t}{\mu}, \tag{18}$$

$$\Delta H^+_{\text{crossflow}} = \max(0.1066 - \Delta H_{\text{crossflow}}, 0), \tag{19}$$

$$f(\Delta H^+_{\text{crossflow}}) = 6200(\Delta H^+_{\text{crossflow}}) + 50000(\Delta H^+_{\text{crossflow}})^2, \tag{20}$$

$$\Delta H^-_{\text{crossflow}} = \max(-(0.1066 - \Delta H_{\text{crossflow}}), 0), \tag{21}$$

$$f(\Delta H^-_{\text{crossflow}}) = 75\tanh\left(\frac{\Delta H^-_{\text{crossflow}}}{0.0125}\right). \tag{22}$$

Helicity, alternatively known as the streamwise vorticity $\Omega_{\text{streamwise}}$, is the magnitude of the scalar product of the local values of the unit velocity vector, $\vec{U}$, and vorticity vector, $\vec{\Omega}$:

$$\vec{U} = \left(\frac{u}{\sqrt{u^2 + v^2 + w^2}}, \frac{v}{\sqrt{u^2 + v^2 + w^2}}, \frac{w}{\sqrt{u^2 + v^2 + w^2}}\right), \tag{23}$$

$$\vec{\Omega} = \left(\frac{\partial w}{\partial y} - \frac{\partial v}{\partial z}, \frac{\partial u}{\partial z} - \frac{\partial w}{\partial x}, \frac{\partial v}{\partial x} - \frac{\partial u}{\partial y}\right), \tag{24}$$

and can be represented using the non-dimensional crossflow strength $H_{\text{crossflow}}$ as,

$$\Omega_{\text{streamwise}} = |\vec{U} \cdot \vec{\Omega}|, \tag{25}$$

$$H_{\text{crossflow}} = \frac{d\Omega_{\text{streamwise}}}{U}. \tag{26}$$

B. Intermittency transport equation

The transport equation for intermittency, also non-dimensionalized and written in non-conservative form, is:

$$\frac{\partial \gamma}{\partial t} + u_j \frac{\partial \gamma}{\partial x_j} = P_\gamma - E_\gamma + \frac{1}{Re} \frac{\partial}{\partial x_j}\left[\left(v + \frac{v_t}{\sigma_f}\right)\frac{\partial \gamma}{\partial x_j}\right], \tag{27}$$

$$P_\gamma = c_{a1}F_{\text{length}}F_{\text{onset}}\Omega\sqrt{\gamma}(1 - c_{e1}\gamma), \tag{28}$$

$$F_{\text{onset}} = \max(\sqrt{F_{\text{onset2}} - F_{\text{onset3}}}, 0), \tag{29}$$

$$F_{\text{onset3}} = \max\left(1 - \left(\frac{R_T}{2.5}\right)^3, 0\right), \tag{30}$$

$$F_{\text{onset2}} = \min(\max(F_{\text{onset1}}, F_{\text{onset1}}^4), 2), \tag{31}$$

$$F_{\text{onset1}} = \frac{Re_S}{2.6Re_{\theta c}}, \tag{32}$$

$$c_{e1} = 1.0; \quad c_{a1} = 2.0; \quad \sigma_f = 1.0, \tag{33}$$

$$E_\gamma = c_{a2}F_{\text{turb}}\Omega\gamma(c_{e2}\gamma - 1), \tag{34}$$

$$F_{\text{turb}} = e^{-(\frac{R_T}{4})^4}, \tag{35}$$

$$c_{e2} = 50; \quad c_{a2} = 0.06. \tag{36}$$

The F_{length} and $Re_{\theta c}$ correlations are as follows:

$$F_{\text{length}} = \begin{cases} 398.189 \cdot 10^{-1} + (-119.270 \cdot 10^{-4})\tilde{Re}_{\theta t} + (-132.567 \cdot 10^{-6})\tilde{Re}_{\theta t}^2 & \tilde{Re}_{\theta t} < 400, \\[2mm] 263.404 + (-123.939 \cdot 10^{-2})\tilde{Re}_{\theta t} + (194.548 \cdot 10^{-5})\tilde{Re}_{\theta t}^2 + (-101.695 \cdot 10^{-8})\tilde{Re}_{\theta t}^3 & 400 \le \tilde{Re}_{\theta t} < 596, \\[2mm] 0.5 - (\tilde{Re}_{\theta t} - 596.0) \cdot 3 \cdot 10^{-4} & 596 \le \tilde{Re}_{\theta t} < 1200, \\[2mm] 0.3188 & 1200 \le \tilde{Re}_{\theta t}, \end{cases} \tag{37}$$

$$Re_{\theta c} = \begin{cases} \tilde{Re}_{\theta t} - (396.035 \cdot 10^{-2} + (-120.656 \cdot 10^{-4})\tilde{Re}_{\theta t} + (868.230 \cdot 10^{-6})\tilde{Re}_{\theta t}^2 \\ \quad + (-696.506 \cdot 10^{-9})\tilde{Re}_{\theta t}^3 + (174.105 \cdot 10^{-12})\tilde{Re}_{\theta t}^4) & \tilde{Re}_{\theta t} \le 1870, \\[2mm] \tilde{Re}_{\theta t} - (593.11 + 0.482(\tilde{Re}_{\theta t} - 1870.0)) & \tilde{Re}_{\theta t} > 1870. \end{cases} \tag{38}$$

C. Coupling to SA turbulence model

The *SA-neg-noft2* variant of the SA turbulence model [36, 54] was used in the current work and is presented in non-conservative, non-dimensional form below:

$$\frac{\partial\tilde{\nu}}{\partial t} + u_j\frac{\partial\tilde{\nu}}{\partial x_j} = P_{\tilde{\nu}} - D_{\tilde{\nu}} + \frac{1}{\sigma Re}\left[\frac{\partial}{\partial x_j}\left((\nu + \tilde{\nu})\frac{\partial\tilde{\nu}}{\partial x_j}\right) + c_{b2}\frac{\partial\tilde{\nu}}{\partial x_i}\frac{\partial\tilde{\nu}}{\partial x_i}\right], \tag{39}$$

$$P_{\tilde{\nu}} = \frac{c_{b1}}{Re}\tilde{S}\tilde{\nu}; \quad D_{\tilde{\nu}} = \frac{c_{w1}f_w}{Re}\left(\frac{\tilde{\nu}}{d}\right)^2. \tag{40}$$

Osusky [55] presents the non-dimensionalization procedure for the SA turbulence model, which is consistent with that used for the Navier-Stokes equations. The transition model is coupled to the production term, $P_{\tilde{\nu}}$, through the following:

$$\tilde{P}_{\tilde{\nu}} = \gamma P_{\tilde{\nu}}. \tag{41}$$

III. SA-sLM2015 Transition Model

The LM2015 and SA-LM2015 models contain several non-smooth functions in the form of min/max operators and conditional statements. These non-smooth functions, referred to as simple kinks [56, 57], produce discontinuities in the Jacobian. This presents a problem for both the Newton-Krylov solution algorithm and the discrete-adjoint gradient-based optimization algorithm. In the current work, this has been addressed through the application of smooth approximations to min/max operators and conditional statements. In addition, modifications are introduced, such as new F_{onset} and F_{turb} functions, in order to reduce numerical stiffness.

The modifications below describe the simplification and smoothing of the SA-LM2015 transition model, presented in Section II. For the remainder of this work it will be designated SA-sLM2015.

A. Minimum/maximum operators

Several examples of smooth approximations to minimum and maximum operators can be found in the literature. Rivest [58] suggested using a generalized mean-value operator, such as the p-mean:

$$\phi_p(x) \triangleq \frac{\left(\sum_i^n (g_i(x))^p\right)^{\frac{1}{p}}}{n}. \tag{42}$$

As p approaches positive and negative infinity, we recover the maximum and minimum operators, respectively. However, this approximation only holds if $g = (g_1, ..., g_n)$ is a vector of positive real numbers, which limits its applicability. Another approach is to use an exponential penalty function [59–61], defined as:

$$\phi_p(x) \triangleq \frac{\log\left(\sum_i^n \exp(pg_i(x))\right)}{p}. \tag{43}$$

Again, as p approaches positive infinity, the function produces the maximum of g_i, while p approaching negative infinity produces the minimum.

The advantage of this approach is that $g = (g_1, ..., g_n)$ can be a vector of any real numbers. A drawback is the presence of log and exponential functions, which can increase the computational cost. This is especially true as g_i approaches values close to zero. This can introduce denormalized floating point numbers which significantly slow the algorithm. To prevent this, a proximity switch has been developed (Equation 43) to activate the exponential penalty function only in the region near the discontinuity. In addition, when considering a two-variable array the exponential penalty function can be rewritten as:

$$\phi_p(x) \triangleq g_1(x) + \frac{\log\left(1 + \exp(p(g_2(x) - g_1(x)))\right)}{p}. \tag{44}$$

In combination with the proximity switch, this form of the exponential penalty function prevents both underflow and overflow. The proximity switch is given by:

Algorithm 1 Smooth maximum/minimum function of two variables

1: **function** $\phi_p(g_1(x), g_2(x))$
2:     $p_{\text{switch}} \leftarrow 10^{-15}$ ▷ Cutoff value for proximity check
3:     $a \leftarrow \max(g_1(x), g_2(x))$ ▷ Save larger value
4:     $b \leftarrow \min(g_1(x), g_2(x))$ ▷ Save smaller value
5:     **if** $p > 0$ **then**   ▷ Determine maximum
6:         **if** $|a - b| > -\frac{\log(|p| \cdot p_{\text{switch}})}{|p|}$ **then**   ▷ Proximity switch
7:             $\phi_p(x) \leftarrow a$ ▷ Return maximum
8:             **return**
9:         **else**
10:            $\phi_p(x) \leftarrow \left(a + \frac{\log(1+\exp(p(b-a)))}{p} \right)$ ▷ Calculate exponential penalty function
11:    **else**   ▷ Determine minimum
12:        **if** $|a - b| > -\frac{\log(|p| \cdot p_{\text{switch}})}{|p|}$ **then**   ▷ Proximity switch
13:            $\phi_p(x) \leftarrow b$ ▷ Return minimum
14:            **return**
15:        **else**
16:            $\phi_p(x) \leftarrow \left(b + \frac{\log(1+\exp(p(a-b)))}{p} \right)$ ▷ Calculate exponential penalty function

---

$$\phi_{\text{switch}} \triangleq -\frac{\log(|p| \cdot p_{\text{switch}})}{|p|}, \tag{45}$$

where p_{switch} represents a cutoff value for the proximity check, which for the current work is set to a value of 10^{-15}. If the magnitude of the difference between the two variables, $|g_1(x) - g_2(x)|$, is greater than ϕ_{switch}, demonstrating we are far from the discontinuity, a simple min/max operator is used. As we approach the kink, if the difference between the two variables is less than ϕ_{switch}, the exponential penalty function is used.

Algorithm 1 presents the complete method for approximating a minimum/maximum operator, based on the value of the smoothing parameter, p, for two variables, $g_1(x)$ and $g_2(x)$, using the exponential penalty functions including the proximity switch. Figure 1 illustrates the effect of this smoothing by approximating the maximum of a variable and a constant using various smoothing values, p. For large values of p the region of smoothing is small, and the sharp region is closely modelled. As p is reduced, the domain where the exponential penalty functions are active increases, increasing computational cost and producing a smoother approximation of the kink region. Although adaptively updating the value of p has been shown to help prevent ill-conditioned systems [60], all min/max operators present in the SA-sLM2015 model were approximated using this algorithm with fixed magnitudes of p of 300, $\phi_{\pm 300}$, which was found through numerical experimentation to provide a good balance between convergence properties and solution accuracy.

B. Intermittency Source Terms

1. F_{onset}

The F_{onset} function (Equations 29-32) couples the SA, intermittency, and momentum-thickness Reynolds number equations. It was developed using several layers of minimum and maximum operators to activate the production of intermittency in the boundary layer, triggering the transition process. Solving the mean flow, turbulence, and transition
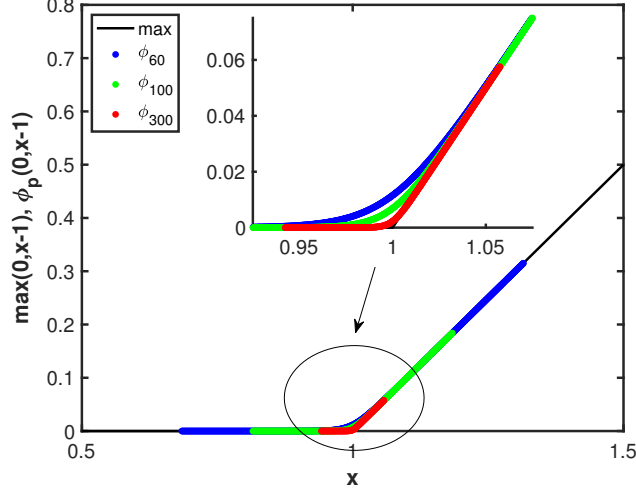
Fig. 1 $\max(0, x - 1)$ **approximated using** ϕ_p **with various values for** p.

equations in a fully-coupled manner results in the F_{onset} function being particularly problematic, and often the bottleneck in flow solver convergence. Rashad [62] investigated the design space of several transition region models and noted that the smoothness of the ramp-up of the eddy-viscosity was found to be particularly important to the smoothness of the design space. He also demonstrated the importance of achieving deep numerical convergence of the transition model residual. Therefore, special care was taken in ensuring that the F_{onset} function be as smooth as possible, while maintaining the same characteristics of the original function.

The transition process is triggered when F_{onset1} (Equation 32) exceeds unity, and is sustained as the eddy-viscosity ratio increases. To smooth and simplify this process the F_{onset} function was reformulated using a hyperbolic tangent function as follows:

$$F_{\text{onset1}} = \sqrt{\left(\frac{Re_S}{2.6Re_{\theta c}}\right)^2 + \left(R_T\right)^2},$$ (46)

$$F_{\text{onset}} = \frac{\tanh(6(F_{\text{onset1}} - 1.35)) + 1}{2}.$$ (47)

Similar to the original, the new F_{onset} function is activated when F_{onset1} exceeds unity; however, once a turbulent boundary layer has formed F_{onset1} remains active. This increases the stability of the model around laminar separation bubbles, where the solution can oscillate as the bubble grows and shrinks, but prevents the model from being able to predict relaminarization. For flight conditions typical of transport aircraft we do not expect relaminarization to occur; however, the reader should be aware of this limitation.

2. F_{turb}

In the SA-LM2015 model the F_{turb} function (Equation 35) remains active until a threshold eddy viscosity ratio is reached, approximately a value of 4. Until this threshold value is reached, the destruction term remains active and
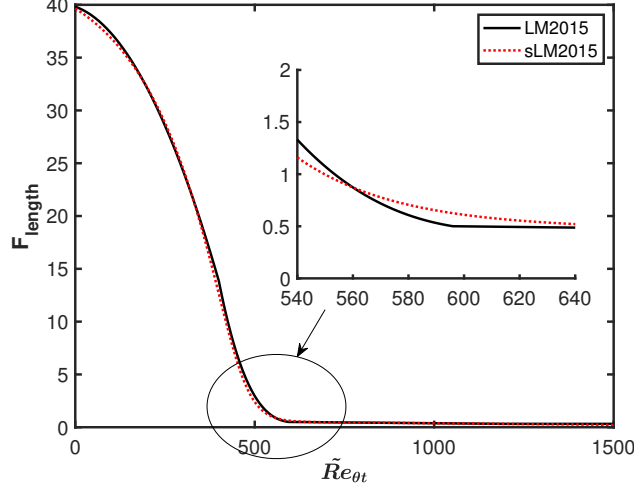
Fig. 2   Original and smooth F_{length} functions.

interferes with the production term, slowing convergence and often producing oscillations. To remedy this, a new function was developed which deactivates the destruction term when F_{onset} becomes active, and rapidly deactivates F_{turb} as turbulent eddy viscosity, R_T, is produced. It is given as follows,

$$F_{\text{turb}} = (1 - F_{\text{onset}}) \exp(-R_T). \tag{48}$$

3. F_{length}

The original F_{length} function (Equation 37) consists of conditional statements and is non-differentiable at the boundaries. In the current work, this is avoided by approximating F_{length} using a modified, flexible version of a sigmoid function known as a generalized logistic function [63]. The new F_{length} function is defined below and plotted in Figure 2:

$$F_{\text{length1}} = \exp(-3 \cdot 10^{-2} (\tilde{R}e_{\theta t} - 460)), \tag{49}$$

$$F_{\text{length}} = 44 - \frac{44 - (0.50 - 3 \cdot 10^{-4} (\tilde{R}e_{\theta t} - 596))}{(1 + F_{\text{length1}})^{\frac{1}{6}}}. \tag{50}$$

4. $Re_{\theta c}$

In previous work approximations of the critical momentum-thickness Reynolds number, $Re_{\theta c}$, as linear functions of $\tilde{R}e_{\theta t}$ are introduced [47, 48, 50]. In the current work a sinusoidal approximation is developed in order to better represent the lower $\tilde{R}e_{\theta t}$ behaviour of the original correlation (Equation 38). The critical momentum-thickness Reynolds number is simplified from the original version as follows:

$$Re_{\theta c} = 0.67 \tilde{R}e_{\theta t} + 24 \sin\left(\frac{\tilde{R}e_{\theta t}}{240} + 0.5\right) + 14. \tag{51}$$

The original and smooth $Re_{\theta c}$ functions are plotted in Figure 3. For large values of $\tilde{R}e_{\theta t}$ the new correlation produces smaller $Re_{\theta c}$ values relative to the original model; however this difference has been accounted for in the model
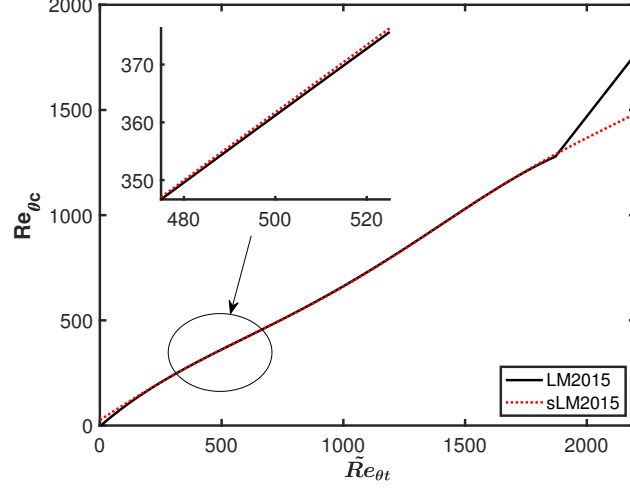
Fig. 3 Original and smooth $Re_{\theta c}$ functions.

calibration.

5. P_γ and E_γ

The maximum value of vorticity magnitude in the intermittency production and destruction terms, P_γ (Equation 28) and E_γ (Equation 34), was limited to improve stability. Vorticity magnitude is included to obtain the correct dimensions for the source terms; however, it was found that large values of vorticity, especially near laminar separation bubbles, can lead to the solution oscillating. Limiting the maximum vorticity value in the intermittency source terms restricts the relative magnitude of the sources, improving the numerical behaviour of the model. The limiting is a function of the freestream Mach number in order to account for the non-dimensionalization of velocity by the speed of sound, a_∞, and the freestream Reynolds number to account for the scaling of vorticity in laminar boundary layers with respect to the square root of the Reynolds number. The Reynolds number is multiplied by the Mach number to recover the Reynolds number based on the freestream velocity. It is important to note that while the presence of the Mach number is the result of the particular non-dimensionalization used, the square root of the freestream Reynolds number based on the freestream velocity is a physical scaling that is independent of the non-dimensionalization. Furthermore, the vorticity limiting is introduced only to improve the numerical behaviour of the model and does not aim to improve its predictive capability. The new source terms are given as follows,

$$P_\gamma = c_{a1} F_{\text{length}} F_{\text{onset}} \left[\phi_{-300} \left(\Omega, \frac{M\sqrt{MRe}}{20} \right) \right] \sqrt{\gamma} (1 - c_{e1}\gamma), \tag{52}$$

$$E_\gamma = c_{a2} F_{\text{turb}} \left[\phi_{-300} \left(\Omega, \frac{M\sqrt{MRe}}{20} \right) \right] \gamma (c_{e2}\gamma - 1), \tag{53}$$

and are illustrated in Figures 4 (a-d) alongside the original SA-LM2015 source terms. The total source terms, $S_\gamma = P_\gamma - E_\gamma$, are plotted with fixed F_{length} and vorticity magnitude, Ω, values of unity versus the transition criterion
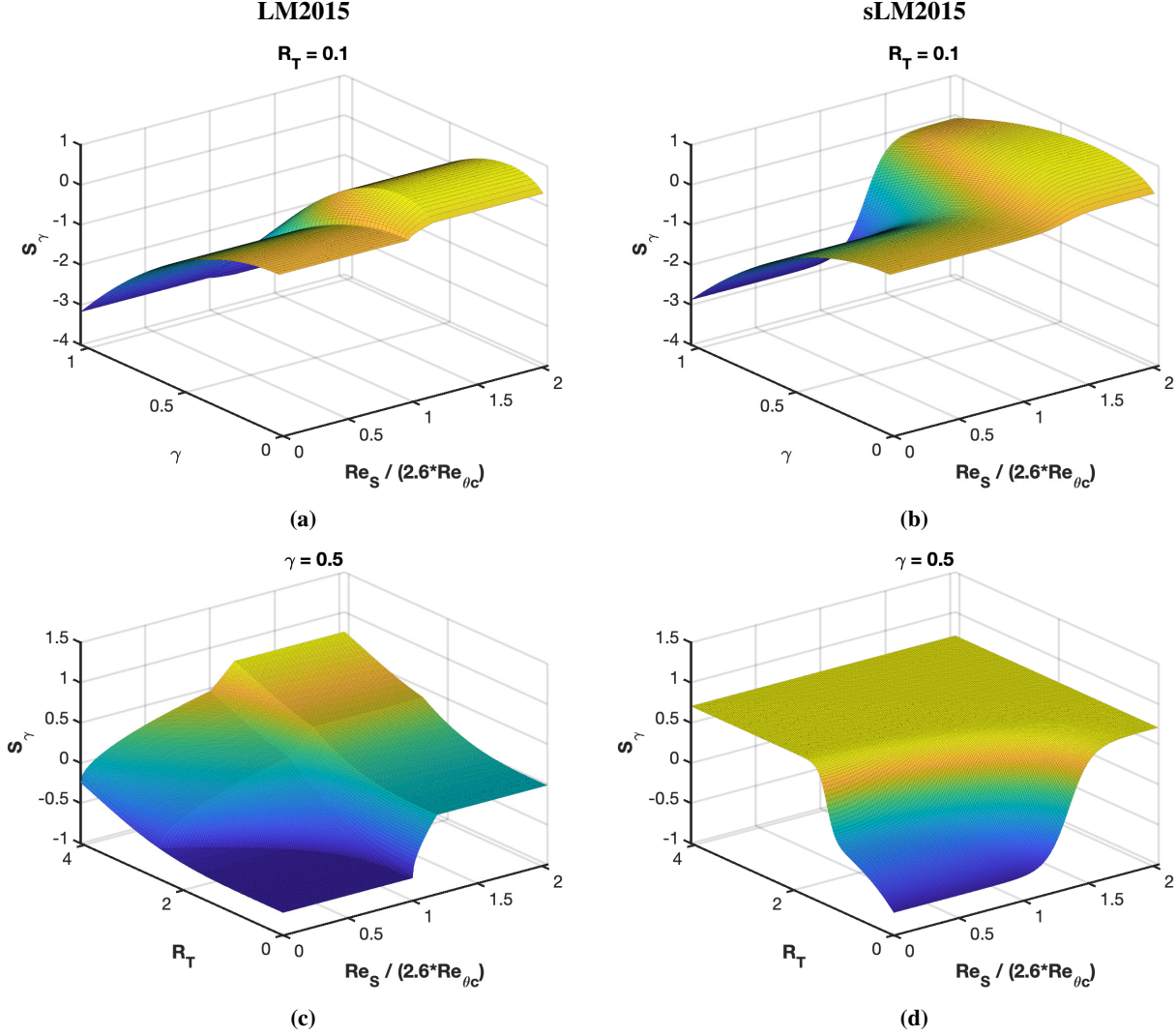
14

Fig. 4 **Original and smooth intermittency source terms,** $S_\gamma = P_\gamma - E_\gamma$**, plotted versus the transition criterion (Equation 32), intermittency,** γ**, and the eddy viscosity ratio,** R_T**, with** $F_{\text{length}} = \Omega = 1$**.**

(Equation 32), intermittency, γ, and the eddy viscosity ratio, R_T. The reformulated intermittency source terms provide a smoother design space, while the results in Section V demonstrate that the predicted transition locations with these modifications match well with the SA-LM2015 model and with experiment.

C. Momentum-thickness Reynolds number Empirical Correlations

1. $F(\lambda_\theta)$

Similar to the F_{length} function, the $F(\lambda_\theta)$ correlations (Equation 9) are conditional, depending on the sign of the pressure gradient parameter, λ_θ. Here $F(\lambda_\theta)$ is approximated using exponential penalty functions:

$$F(\lambda_\theta)_1 = 1 + 0.275[1 - e^{[-35\lambda_\theta]}]e^{-[\frac{Tu}{0.5}]},$$
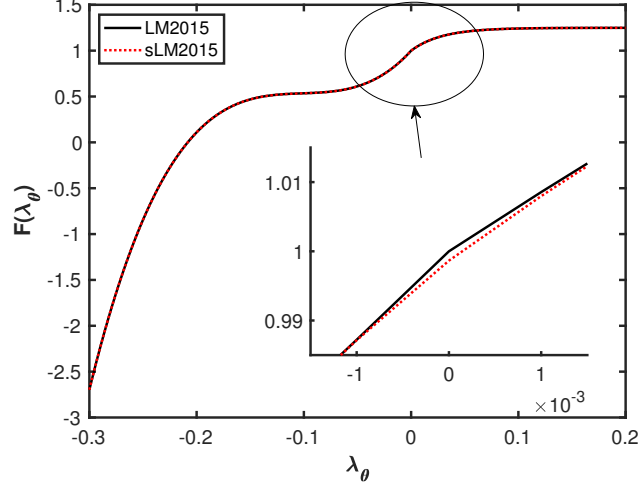
(54)

Fig. 5 Original and smooth $F(\lambda_\theta)$ functions for a turbulence intensity of 0.05%.

$$F(\lambda_\theta)_2 = \phi_{300}(F(\lambda_\theta)_1, 1), \tag{55}$$

$$F(\lambda_\theta)_3 = 1 - [-12.986\lambda_\theta - 123.66\lambda_\theta^2 - 405.689\lambda_\theta^3]e^{-[\frac{Tu}{1.5}]^{1.5}}, \tag{56}$$

$$F(\lambda_\theta) = \phi_{-300}(F(\lambda_\theta)_2, F(\lambda_\theta)_3). \tag{57}$$

The original and smooth $F(\lambda_\theta)$ functions are plotted in Figure 5.

IV. Solution Algorithm

A. Parallel Newton-Krylov-Schur flow solver

An efficient, robust, and accurate flow solver is crucial to the performance of an optimization algorithm, as flow analysis is conducted many times over the course of the optimization process, with a variety of geometries expected. The flow solver used in the current work is a three-dimensional multi-block structured finite-difference solver developed by Hicken and Zingg [64] for the solution of the Euler equations, and extended to the RANS equations coupled to the one-equation SA turbulence model by Osusky and Zingg [65]. The governing equations are spatially discretized using summation-by-parts operators, with simultaneous approximation terms applied to enforce boundary conditions and inter-block coupling. To decrease the computational time required to complete a flow solution, the computational domain is decomposed into multiple blocks, resulting in multi-block structured grids, which allow for efficient parallel computations.

A fully-coupled, implicit Newton-Krylov-Schur solution algorithm making use of a pseudo-transient continuation strategy is applied to the set of nonlinear algebraic equations produced by the spatial discretization of the governing equations to drive the solution from an initial guess to a converged steady-state solution. The solution strategy consists of two phases, an approximate-Newton phase followed by an inexact-Newton phase. Globalization is achieved using the

16

approximate-Newton phase, where an implicit Euler time marching strategy with local time linearization is applied using an approximate, analytically derived Jacobian. After the residual drops several orders of magnitude, Newton's method using a full second-order Jacobian, formed either analytically or using a forward difference, is used to converge the system to a residual norm of machine zero. The large system of linear equations generated at each iteration in both phases is solved using the GMRES linear solver [66], preconditioned using an approximate-Schur parallel preconditioner [67].

B. Considerations for SA-LM2015 and SA-sLM2015 transition models

Unless suitable steps are taken to modify the basic algorithm, the implementation of the SA-LM2015 and SA-sLM2015 transition model equations in a Newton-Krylov solver can lead to numerical instability. The source terms in the γ-$\tilde{R}e_{\theta t}$ equations are large and highly non-linear. This leads to numerical stiffness through the presence of restrictive source-term time scales [68, 69]. Several authors [68, 70, 71] have suggested that fully-implicit approaches can lead to numerical instabilities due to the formation of Jacobians with unfavourable characteristics. More specifically, it has been demonstrated that the implicit treatment of sources can lead to unbounded solution updates, and that a modified explicit treatment of sources can improve solver performance [69]. Additionally, recent work has suggested that fully-coupled approaches may lead to reduced performance due to increased numerical stiffness [72–74]. It has been shown that relaxing the coupling between the turbulence and mean-flow, or transition and turbulence equations, can reduce this stiffness, leading to reduced computational cost [74], and improved convergence [72, 73].

However, the rate of convergence of Newton's method is closely linked to the the accuracy of the Jacobian. Neglecting terms or otherwise manipulating the Jacobian can prevent quadratic convergence [75]. Yildirim et al. [76] demonstrated that segregating the turbulence model in an approximate-Newton phase to globalize Newton's method can be effective for fully-turbulent simulations. Similar approaches have been investigated for the SA-LM2015 and SA-sLM2015 models; however, this can result in the solution stalling in the approximate-Newton phase. The transition model equations require a tight coupling in order to achieve deep convergence, often requiring stricter linear solver tolerances relative to fully-turbulent simulations. Moreover, the transition model source terms remain active throughout the inexact-Newton phase. Rather than modifying the Jacobian matrix, Lian et al. [69] demonstrated that restricting the local time step based on the non-dimensional source-term number, defined as the product of the largest positive eigenvalue of the source-term Jacobian matrix and the local time step, can be an effective way of stabilizing large sources in a fully-coupled, implicit algorithm. A source-term time step restriction based on the ideas developed by Lian et al. [69] has been implemented in the current work.

Additional modifications to the Newton-Krylov algorithm were implemented to improve robustness. These include equation and variable scaling measures, a solution update damping routine, and an unsteady line-search backtracking algorithm.

17

1. Equation and variable scaling

The turbulence and transition model variables can vary significantly in magnitude from the mean-flow variables and do not contain inherent geometric scaling [75]. In addition, large off-diagonal entries are introduced through the linearization of the turbulence and transition model equations with respect to the mean flow variables. If not accounted for, these factors can result in improper scaling of the linear system and poor performance of the linear solver. To address this, row and column scaling measures, including residual auto scaling, are used based on the work by Chisholm and Zingg [75] and Osusky and Zingg [55, 65]. Instead of solving the linear system of equations directly, a scaled version of the equations is solved, given by:

$$S_a S_r \left(\frac{\mathcal{I}}{\Delta t} + \mathcal{A}^{(n)} \right) S_c S_c^{-1} \Delta \mathcal{Q}^{(n)} = -S_a S_r \mathcal{R}^{(n)}, \tag{58}$$

where S_a represents the residual auto-scaling matrix and

$$S_{ri} = \begin{bmatrix} J_i^{\frac{2}{3}} & & & & \\ & \ddots & & & \\ & & J_i^{\frac{2}{3}} & & \\ & & & \tilde{\nu}_{\max}^{-1} J_i^{\frac{-1}{3}} & \\ & & & & \gamma_{\max}^{-1} J_i^{\frac{-1}{3}} & \\ & & & & & \tilde{Re}_{\theta t \max}^{-1} J_i^{\frac{-1}{3}} \end{bmatrix}, \quad S_{ci} = \begin{bmatrix} 1 & & & & \\ & \ddots & & & \\ & & 1 & & \\ & & & \tilde{\nu}_{\max} & \\ & & & & \gamma_{\max} & \\ & & & & & \tilde{Re}_{\theta t \max} \end{bmatrix},$$

are the ith blocks of the diagonal row and column scaling matrices, respectively. Through a thorough algorithm optimization procedure, Osusky and Zingg [65] determined an optimal normalization value for $\tilde{\nu}_{\max}$ of 10^3, which accounts for the maximum turbulence value that is likely to be encountered in the flow solve. Following a similar approach, $\gamma_{\max}$ and $\tilde{Re}_{\theta t \max}$ values of 10 and 10^4, respectively, were selected. The partially scaled residual, $S_r \mathcal{R}^{(n)}$, is used when monitoring convergence. Full details on the auto, row, and column scaling measures can be found in Osusky and Zingg [55, 65].

2. Solution update

The transition model equations can become unstable if the intermittency and transition onset momentum-thickness Reynolds number are not bounded. Solution-limited time stepping methods, such as those developed by Chisholm and Zingg [75], and Lian et al. [69, 77], were investigated. However these methods can slow convergence for cases with stable updates and lead to restrictive time steps for variables approaching zero. In order to ensure stable physical transition model updates, a solution update damping procedure was implemented, as described in Algorithm 2. Clipping

Algorithm 2 Transition model solution update damping

1: $\theta_{\text{fac}} \leftarrow 0.99$	▷ Damping factor
2: **for** $j = 1, n_{\text{nodes}}$ **do**	▷ Loop over local nodes
3: **for** $l = 1, n_{\text{var}}$ **do**	▷ Loop over variables
4: $\mathcal{Q}_{j,l}^{(n+1)} = \mathcal{Q}_{j,l}^{(n)} + \Delta\mathcal{Q}_{j,l}^{(n)}$	▷ Update solution
5: $m = 0$	▷ Initialize count variable
6: **while** $\mathcal{Q}_{j,7}^{(n+1)} > 2$ **or** $\mathcal{Q}_{j,7}^{(n+1)} < 10^{-10}$ **do**	▷ Limit intermittency
7: $m = m + 1$	▷ Count number of damping iterations
8: $\mathcal{Q}_{j,7}^{(n+1)} = \mathcal{Q}_{j,7}^{(n)} + (\theta_{\text{fac}})^m \Delta\mathcal{Q}_{j,7}^{(n)}$	▷ Damp update
9: $m = 0$	▷ Initialize count variable
10: **while** $\mathcal{Q}_{j,8}^{(n+1)} < 20$ **do**	▷ Limit $\tilde{Re}_{\theta t}$
11: $m = m + 1$	▷ Count number of damping iterations
12: $\mathcal{Q}_{j,8}^{(n+1)} = \mathcal{Q}_{j,8}^{(n)} + (\theta_{\text{fac}})^m \Delta\mathcal{Q}_{j,8}^{(n)}$	▷ Damp update

the transition model variables at these bounds was also investigated; however placing a hard limit on variable bounds can potentially lead to stalling of the nonlinear solver. It is important to note that with the implementation of the source-term time stepping strategy, which prevents unstable solution updates, in combination with a more dissipative first-order upwind discretization strategy for the SA, SA-LM2015, and SA-sLM2015 equations, the upper and lower bounds specified in Algorithm 2 are rarely reached. Furthermore, steady-state solutions for intermittency respect the bounds of 0.02 and 1 implicitly defined in the source terms. In addition to the solution update damping, a backtracking line-search method was implemented based on the work of Modisette [78]

3. Source-term time stepping

Lian et al. [69] demonstrated that an implicit scheme becomes unstable with source-term time step values greater than unity. Maintaining a source-term time step less than unity can prevent unbounded solution updates, where the source-term time step is determined by the product of the largest positive eigenvalue of the source-term Jacobian matrix, $\mathcal{A}_{\text{source}}$, and the local time step, $\lambda_{\text{source}}\Delta t_{j,k,m}^{(n)}$. For the current work the eigenvalues of the block diagonal source-term Jacobian are determined using a QR algorithm. The local time step is restricted to ensure the following source-term time step condition is met:

$$\mathcal{A}_{\text{source}} = \begin{bmatrix} \dfrac{\partial \mathcal{S}_{\tilde{\nu}}}{\partial \tilde{\nu}} & \dfrac{\partial \mathcal{S}_{\tilde{\nu}}}{\partial \gamma} & \dfrac{\partial \mathcal{S}_{\tilde{\nu}}}{\partial \tilde{Re}_{\theta t}} \\[2ex] \dfrac{\partial \mathcal{S}_{\gamma}}{\partial \tilde{\nu}} & \dfrac{\partial \mathcal{S}_{\gamma}}{\partial \gamma} & \dfrac{\partial \mathcal{S}_{\gamma}}{\partial \tilde{Re}_{\theta t}} \\[2ex] \dfrac{\partial \mathcal{S}_{\tilde{Re}_{\theta t}}}{\partial \tilde{\nu}} & \dfrac{\partial \mathcal{S}_{\tilde{Re}_{\theta t}}}{\partial \gamma} & \dfrac{\partial \mathcal{S}_{\tilde{Re}_{\theta t}}}{\partial \tilde{Re}_{\theta t}} \end{bmatrix},$$

$$\lambda_{\text{source}}\Delta t_{j,k,m}^{(n)} \leq 0.9, \tag{59}$$

where $\mathcal{S}$ represents the local source-term vector, in this case consisting of the SA-LM2015, SA-sLM2015, and SA turbulence model source terms. Several source-term time step values were investigated, however 0.9 was determined

to be an effective balance between speed and robustness. The spatially varying time step and the time step ramping procedure are described in [65].

As demonstrated by Lian et al. [69], source-term eigenvalues can remain large throughout convergence. This can cause the local time step to remain excessively small throughout the solution process, delaying convergence. However, for most cases the large sources are only destabilizing in the early stages of convergence. To accelerate convergence, a switch was developed for deactivating the source-term time stepping in the inexact-Newton phase. The source-term time stepping is active throughout the approximate-Newton phase, and is deactivated after five successive inexact-Newton iterations for which backtracking is not active. Source-term time stepping is reactivated if backtracking is required, or if the relative residual drop (Equation 60) increases beyond the residual drop tolerance for the switch from the approximate- to the inexact-Newton phase, which is typically a value of 10^{-5}.

V. Results

Both transition models, SA-LM2015 and SA-sLM2015, are validated in the following section using a range of two- and three-dimensional transition test cases. These test cases include natural and separation-induced transition as well as transition due to crossflow instabilities, with the results compared to experimental values. Convergence histories are illustrated by the L2-norm of the fully-coupled residual, including the row (equation) scaling measure presented in Section IV, normalized by the initial residual,

$$\mathcal{R}_d^{(n)} = \frac{||\mathcal{R}^{(n)}||_2}{||\mathcal{R}^{(0)}||_2}, \tag{60}$$

versus the computational time in seconds. All simulations were conducted on Intel Skylake processors with a core clock speed of 2.4GHz and one MPI thread per computational block. All results were obtained using a second-order discretization for the mean flow equations with matrix-based dissipation using V_l and V_n values of 0 and a fourth-difference dissipation coefficient of 0.04 [79]. First-order upwinding was used for the SA, SA-LM2015, and SA-sLM2015 models. The same solution algorithm parameters were used for the 2D and 3D cases, respectively, demonstrating the robustness of the solver. These settings are similar to the values recommended by Osusky and Zingg [55], with the settings for the source term time stepping strategy and scaling measures described previously in Section IV.

A. NLF0416 General Aviation Airfoil

The NLF0416 airfoil is a natural-laminar-flow general aviation airfoil designed by Somers [80]. Experimental results of the NLF0416 airfoil were obtained in the low turbulence pressure tunnel (LTPT) at NASA Langley Research Center [80]. Transition locations were measured for several angles of attack at a Mach number of 0.1 and a Reynolds number of 4.0×10^6. The transition mechanisms for these conditions are natural and separation-induced transition. The turbulence intensity in the wind tunnel used for the experimental study was not specified, however a value of Tu = 0.15% was assumed in order to be consistent with results obtained using the Transition Modelling and Predictive

Table 1   TMPCS NLF0416 structured C-grid dimensions [81]

grid level	dimensions	Δs (chord)	average/maximum $y+$
coarse	529×73	4.47×10^{-6}	0.57/1.19
medium	705×97	3.25×10^{-6}	0.51/0.89
fine	1057×145	2.10×10^{-6}	0.26/0.45

Capabilities Seminar (TCMPS) guidelines [81].

The coarse, medium, and fine NLF0416 family of grids provided by the TMPCS were used in the current work [81]. The dimensions of the structured C-grids are presented in Table 1. A grid-refinement study was conducted for the $0°$ angle of attack case using both transition models and is presented in Figure 6. The refinement study demonstrates a clear second-order convergence trend, as the inverse of the number of grid points, N^{-1}, is proportional to the square of the mesh spacing, although they converge to slightly different lift and drag values due to a difference in predicted transition location. Figure 6 also illustrates the computational results obtained using the SA-LM2015 and SA-sLM2015 transition models on the fine grid level compared to experimental values. The results demonstrate that both the SA-LM2015 model and the SA-sLM2015 model do a reasonable job of matching the forces and transition locations from experiment. Figure 6(e) illustrates that both models under-predict drag at low angles of attack; however this is consistent with results obtained from previous studies using variations of the γ-$\tilde{R}e_{\theta t}$ model [48, 82, 83] and does not appear to be caused by incorrect transition point locations.

The residual convergence histories for these cases are presented in Figure 7. For these simulations the grids were split into 8 computational blocks. The convergence histories demonstrate the improved numerical behaviour of the SA-sLM2015 model. At angles of attack of $−6°$ and $−4°$ a large separation bubble forms on the lower surface of the airfoil, increasing the stiffness of the linear system. This is evident in the decreased slope of the residual curve for the SA-sLM2015 model, as each outer inexact-Newton iteration required more inner GMRES linear solver iterations. It should also be noted that small trailing edge-spacings on the C-grids provided by the TMPCS propagated to the far-field of the domain with little splaying, further increasing the stiffness of the linear system and increasing the computational cost of the simulations.

B. S809 Wind Turbine Airfoil

The S809 airfoil is a natural-laminar-flow wind turbine airfoil designed by Somers [84] and studied in the low-turbulence wind tunnel of the Delft University of Technology Low Speed Laboratory. Experimental results for the S809 airfoil were obtained at a Reynolds number of 2.0×10^6 at angles of attack ranging from $0°$ to $9°$. The free-stream turbulence intensity in the wind tunnel varied between $Tu = 0.02\%$ and $Tu = 0.04\%$. For a Reynolds number of 2.0×10^6 and an angle of attack of $0°$, Somers noted that the primary transition mechanism on both the upper and lower
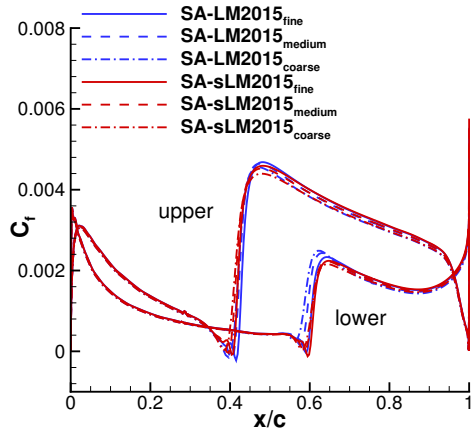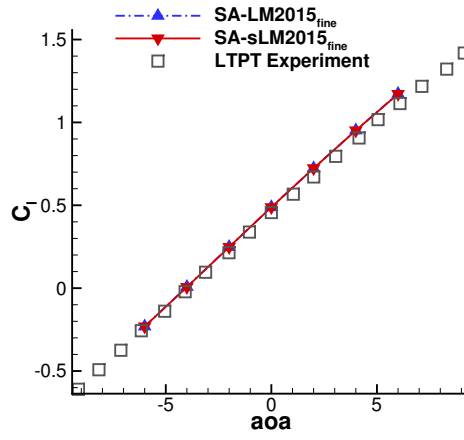
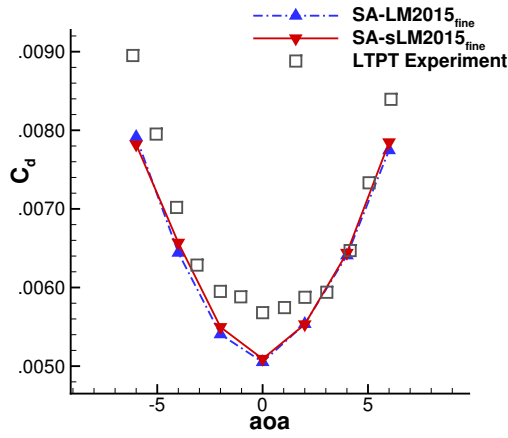(a) Skin friction grid convergence
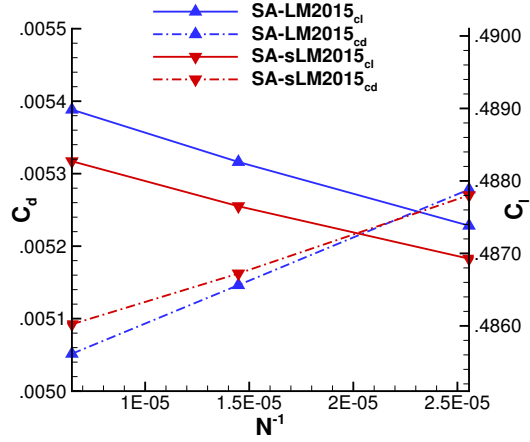
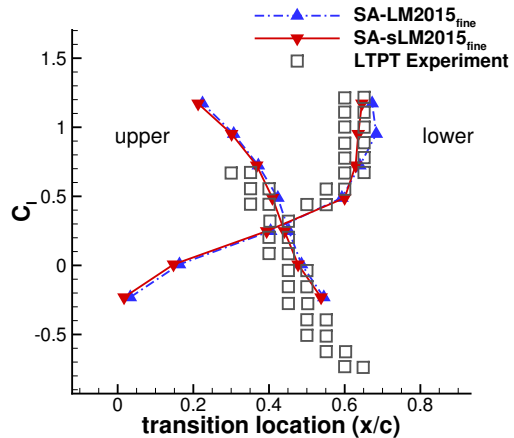(b) Grid convergence for lift and drag
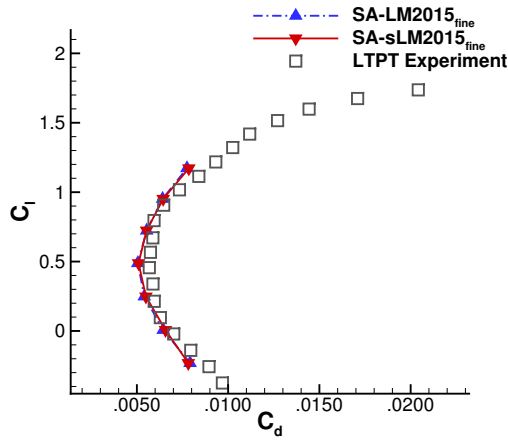
(c) Drag polar

(d) Lift curve

(e) Drag curve

(f) Transition locations

Fig. 6   NLF0416 grid convergence at $0°$ angle of attack, and angle of attack sweep simulated using the SA-LM2015 and SA-sLM2015 transition models at $M = 0.1$, $Re = 4.0 \times 10^6$, and $Tu = 0.15\%$. The 'fine' grid level was used for the sweep, with the experimental results obtained at the LTPT wind tunnel [80].
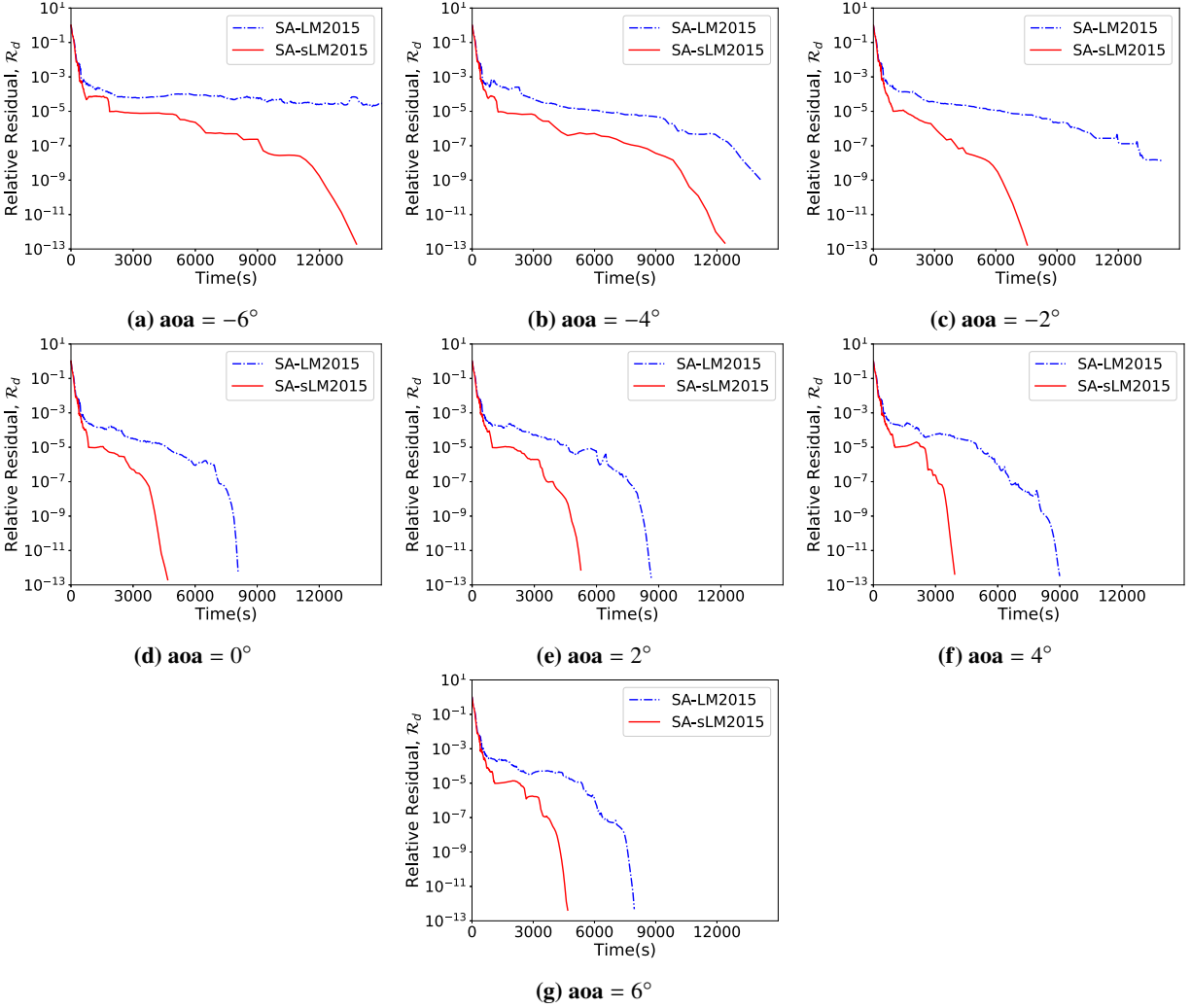
Fig. 7 NLF0416 residual convergence histories for the SA-LM2015 and SA-sLM2015 transition models on the 'fine' grid level split into 8 computational blocks. The airfoil was simulated at $M = 0.1$, $Re = 4.0 \times 10^6$, $Tu = 0.15\%$ and over a range of angles of attack.

surfaces of the airfoil was separation-induced transition due to the presence of large laminar separation bubbles [84]. As the angle of attack increased, the separation bubble on the upper surface decreased in length, disappearing completely at an angle of attack of $5.13°$, with the transition location moving upstream rapidly on the upper surface and the lower surface separation bubble fixing transition near mid-chord over the range of angles of attack. Numerical results were obtained using a Mach number of 0.10, Reynolds number of 2.0×10^6, and a free-stream turbulence intensity of 0.07%, as recommended by the TCMPS guidelines [81].

Computational results were obtained using the S809 grid families supplied through the TCMPS, which were generated using the same conformal mapping method as for the NLF0416 [81], with the coarse, medium, and fine grid dimensions presented in Table 2. A grid-refinement study was conducted for the S809 airfoil at $6°$ angle of attack and is plotted in Figure 8. This condition was chosen as it represents the point beyond the upper corner of the drag

23

Table 2 TMPCS S809 structured C-grid dimensions [81]

grid level	dimensions	Δs (chord)	average/maximum $y+$
coarse	529×73	8.90×10^{-6}	0.60/1.73
medium	705×97	6.47×10^{-6}	0.52/0.81
fine	1057×145	4.19×10^{-6}	0.28/0.54

bucket where the transition location is rapidly moving, which is is expected to amplify the effects of grid refinement on the predictions [81]. Figure 8 also illustrates the forces and transition locations obtained using the SA-LM2015 and SA-sLM2015 transition models on the fine grid level. Although the transition locations match experiment well, both models under-predict drag before and after the upper corner of the drag bucket. Again, this trend has been identified by previous studies using variations of the γ-$\tilde{R}e_{\theta t}$ model [48, 82, 83], as well as studies using the AFT transition model [35, 82], and does not appear to be caused by inaccurate transition prediction.

The residual convergence histories for these cases are presented in Figure 9 for computations using 8 processors. Similar to the NLF0416 airfoil, the large separation bubbles at low angles of attack led to stiff linear systems which slowed convergence. For all angles of attack the SA-sLM2015 model displays substantially improved convergence. In particular, for the 9° angle of attack case the SA-LM2015 model was unable to converge due to the unsteady interaction of the transition model with the laminar separation bubble on the upper surface of the airfoil. This behaviour was also identified by Denison and Pulliam using the LM2015 model [82]. Limiting vorticity in the transition model source terms prevented this oscillation without affecting the accuracy of the solution.

C. NASA NLF2-0415 Infinite Swept Wing

The NASA NLF2-0415 Infinite Swept Wing consists of an NLF2-0415 airfoil extruded with a 45° sweep angle. Experimental measurements were obtained at an angle of attack of −4°, over a range of Mach and Reynolds numbers [85], and including a variety of surface roughness levels [86]. Transition locations were determined using the naphthalene visualization technique. Transition locations for a roughness level, h, of 3.3μm, representing a painted surface, were obtained using the SA-LM2015 and SA-sLM2015 models and are compared with experimental values [86] in Figure 10. The Reynolds number based on free-stream velocity magnitude and chord length was varied from 1.8×10^6 to 3.5×10^6. The free-stream turbulence intensity for the wind tunnel was measured as 0.20%. Transition locations are presented only for the upper surface of the wing, as experimental results are not available for the lower surface.

The computational grid used to obtain these results consists of 270,336 nodes split into 128 blocks, with 90,112 nodes per cross-section, and an off-wall spacing of 2.5×10^{-6} chords, resulting in average and maximum y^+ values of 0.21 and 0.46, respectively. The analytical full Jacobian was used in the inexact-Newton phase for this case and the Tu Braunschweig Sickle Wing. Periodic boundary conditions were used to simulate the infinite swept wing. The results in
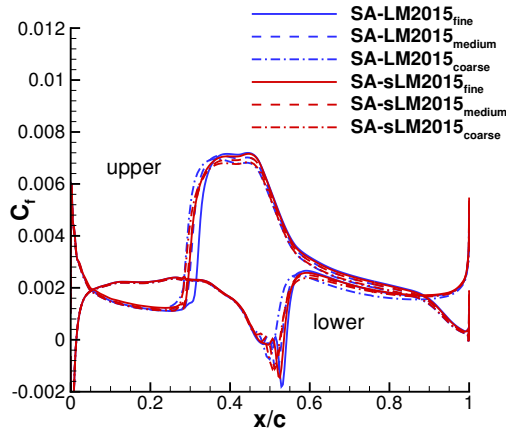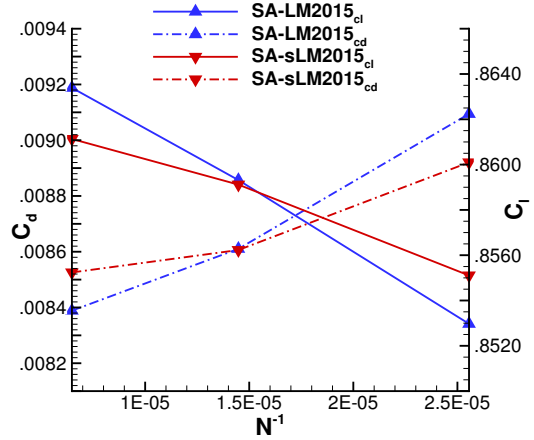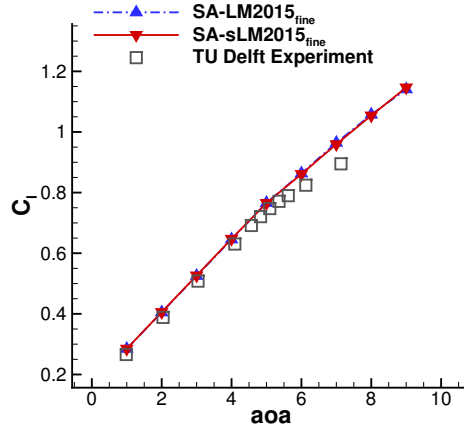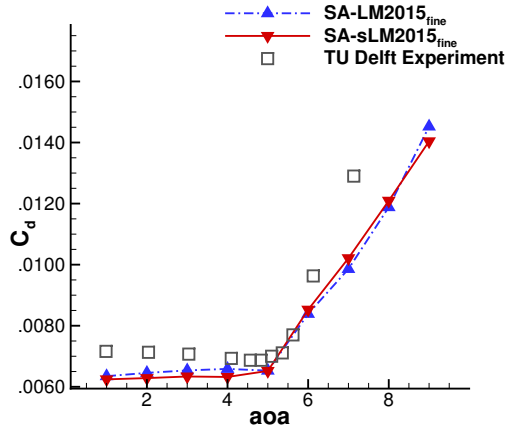
24

(a) Skin friction grid convergence
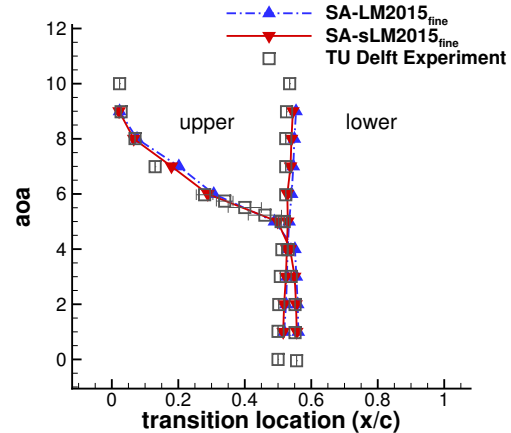

(b) Grid convergence for lift and drag
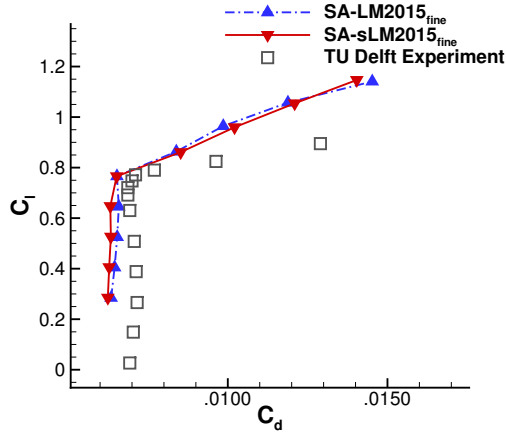
(c) Drag polar

(d) Lift curve

(e) Drag curve

(f) Transition locations

Fig. 8 **S809 grid convergence at** $6°$ **angle of attack, and angle of attack sweep simulated using the SA-LM2015 and SA-sLM2015 transition models at** $M = 0.1$, $Re = 2.0 \times 10^6$, **and** $Tu = 0.07\%$. **The 'fine' grid level was used for the sweep, with the experimental results obtained at the TU Delft wind tunnel [84].**
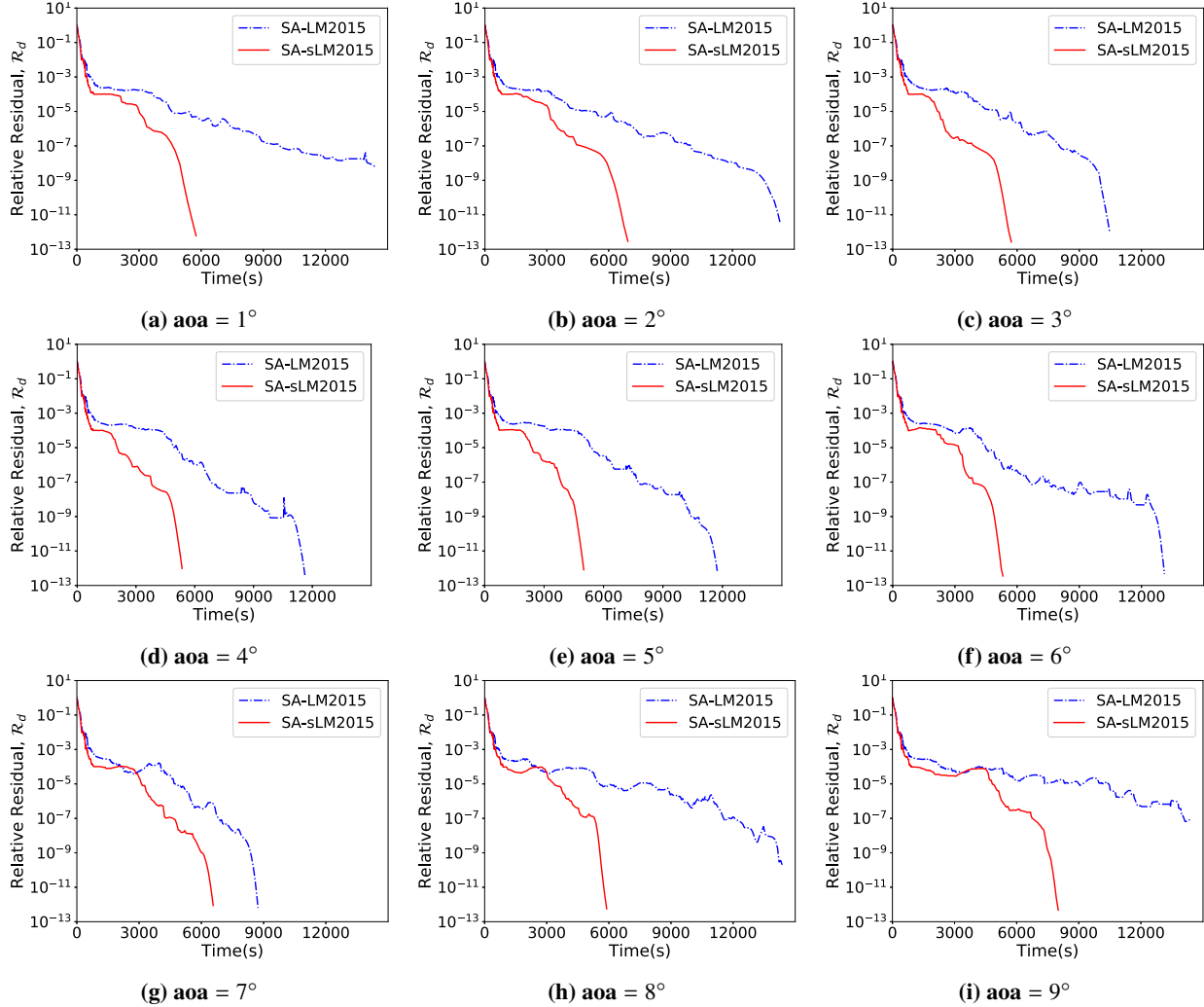
Fig. 9 S809 residual convergence histories for the SA-LM2015 and SA-sLM2015 transition models on the 'fine' grid level split into 8 computational blocks. The airfoil was simulated at $M = 0.1$, $Re = 2.0 \times 10^6$, $Tu = 0.07\%$ and over a range of angles of attack.

Figure 10 demonstrate that both SA-LM2015 and SA-sLM2015 transition models predict transition accurately, while plots of the residual convergence histories in Figure 11 demonstrate that the SA-sLM2015 model provides significantly improved convergence to steady state.

The results demonstrate that the SA-LM2015 model is able to closely predict the location of transition for all Reynolds numbers except for 2×10^6, where there is an error of approximately 14% between the experimental and predicted values. This error is also present in the work of Jung and Baeder [48], where they coupled a semi-local correlation-based transition model formulation with the SA model using the crossflow correlations developed by Muller and Herbst [42], and in the original model developed by Langtry et al. [43]. In the work produced by Radeztsky et al. [86], the results demonstrate that there is significant experimental error associated with this case, which may help to explain this discrepancy.

(a) Transition locations

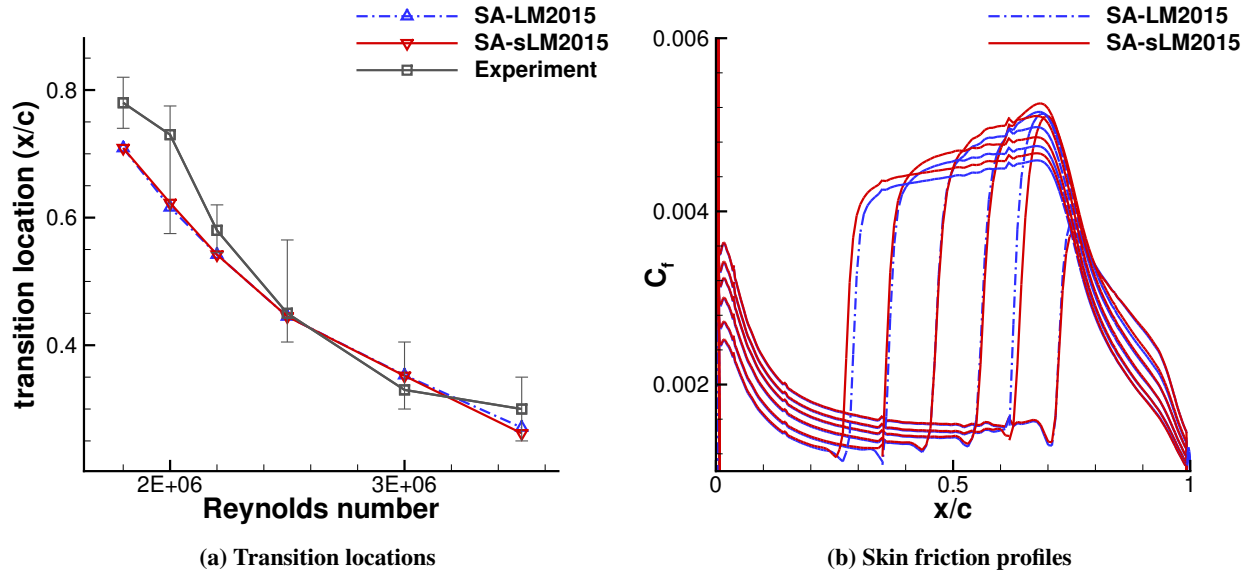**(b) Skin friction profiles**

Fig. 10   Experimental and computational results for the NLF2-0415 infinite swept wing [86] simulated using the SA-LM2015 and SA-sLM2015 transition models at $M = 0.15$, $\alpha = -4°$, $Tu = 0.20\%$, and over a range of Reynolds numbers from $1.8 - 3.5 \times 10^6$.

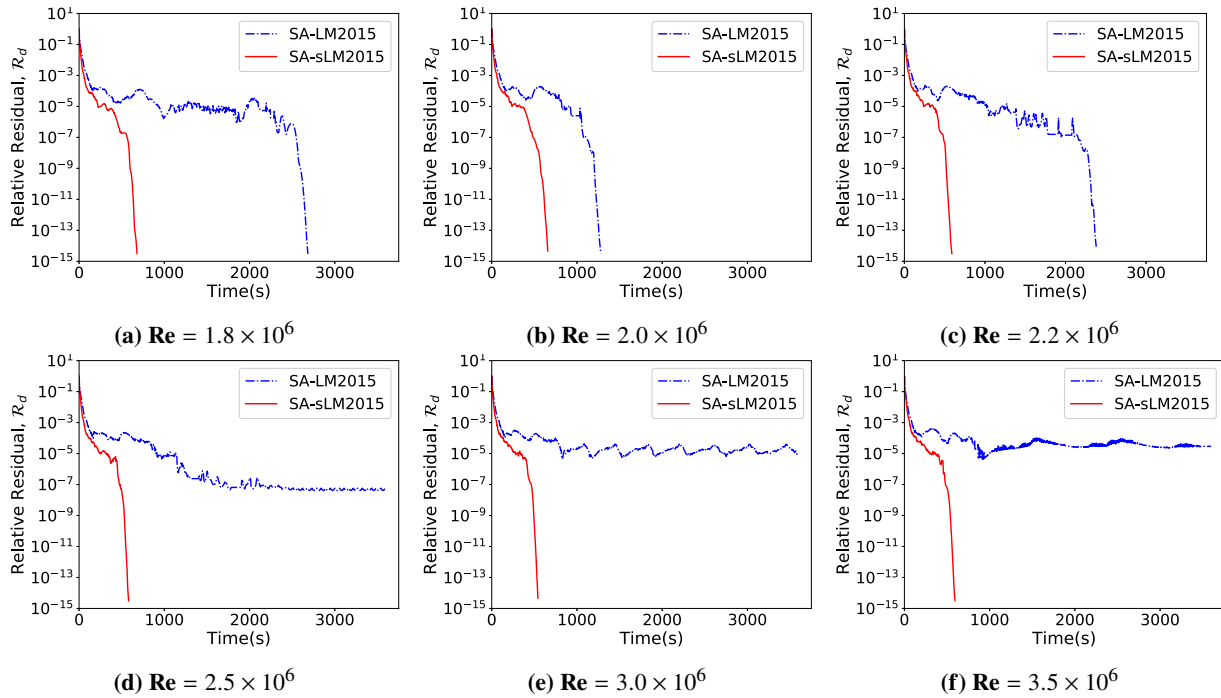
(a) Re $= 1.8 \times 10^6$

(b) Re $= 2.0 \times 10^6$

(c) Re $= 2.2 \times 10^6$

(d) Re $= 2.5 \times 10^6$

(e) Re $= 3.0 \times 10^6$

(f) Re $= 3.5 \times 10^6$

Fig. 11   NLF2-0415 residual convergence histories for the SA-LM2015 and SA-sLM2015 transition models, with the grid split into 128 computational blocks. The infinite swept wing was simulated at $M = 0.15$, $\alpha = -4°$, $Tu = 0.20\%$, and over a range of Reynolds numbers.

It is important to note that the choice of numerical dissipation strongly affects the accuracy of the crossflow transition model. Both the scalar dissipation model developed by Jameson et al. [87] and later refined by Pulliam [88], and

Table 3   Sickle Wing structured O-O grid dimensions

grid level	total node count, N	N-span	N-chord	Δs (chord)	average/maximum $y+$
coarse	2.32×10^6	171	111	7.81×10^{-6}	0.70/2.64
medium	5.19×10^6	217	139	6.02×10^{-6}	0.54/1.55
fine	10.19×10^6	273	175	4.29×10^{-6}	0.39/1.13

the matrix-based dissipation model developed by Swanson and Turkel [79] were investigated for this case. On the mesh used, the scalar dissipation model drastically under predicts the crossflow strength and helicity values. This was determined to be due to the increased dissipation of the scalar dissipation model in and above the laminar boundary layer, which affected the vorticity profile within the boundary layer.

D. TU Braunschweig Sickle Wing

The TU Braunschweig Sickle Wing [89] was developed as a test case for crossflow transition on a complex geometry. The model consists of five main sections designed to create three-dimensional boundary layers with increasing crossflow towards the wing tip. The first section raises the model away from the turbulent boundary layer of the wind tunnel wall, with the three main wing sections swept at 30, 45, and 55° with distinct kinks in the leading edge sweep. As a result, large span-wise gradients are present and the assumptions of linear local stability theory are challenged [89]. The wing is capped with a rounded wing tip. At the experimental flow conditions, the upper surface of the wing has extended regions of strong favourable pressure gradients with crossflow instabilities developing at the section kinks. This results in mixed mode transition scenarios with Tollmien-Schlichting and crossflow instabilities triggering transition, except on the upper surface near the root of the wing, where a laminar separation bubble triggers transition at approximately 80% chord.

The Sickle Wing was simulated at a Reynolds number of 2.75×10^6, Mach number of 0.16, and $-2.6°$ angle of attack. The rms surface roughness of the experimental model was measured to be 1.47μm with a five-point average of the maximum peak to peak height of 9.78μm [89]. In order to be consistent with results obtained using the LM2015 model [43, 44] the surface roughness for the simulations was set to the peak to peak height value of 9.78μm with a free-stream turbulence intensity of 0.17%, which is consistent with the turbulence intensity measured in the wind tunnel [89].

Three levels of O-O topology structured multi-block grids were simulated with the grid details presented in Table 3, including the number of spanwise and chordwise nodes on each of the upper and lower surfaces. Each grid level was split into 592 computational blocks. Figure 12 illustrates the skin friction profiles on the upper and lower surfaces of the Sickle Wing using both the SA-LM2015 and SA-sLM2015 transition models for all three grid levels overlaid with experimental transition locations [89]. Both models predict the transition fronts reasonably well.

As the grid is refined the transition front on the lower surface, which is dominated by natural transition, moves
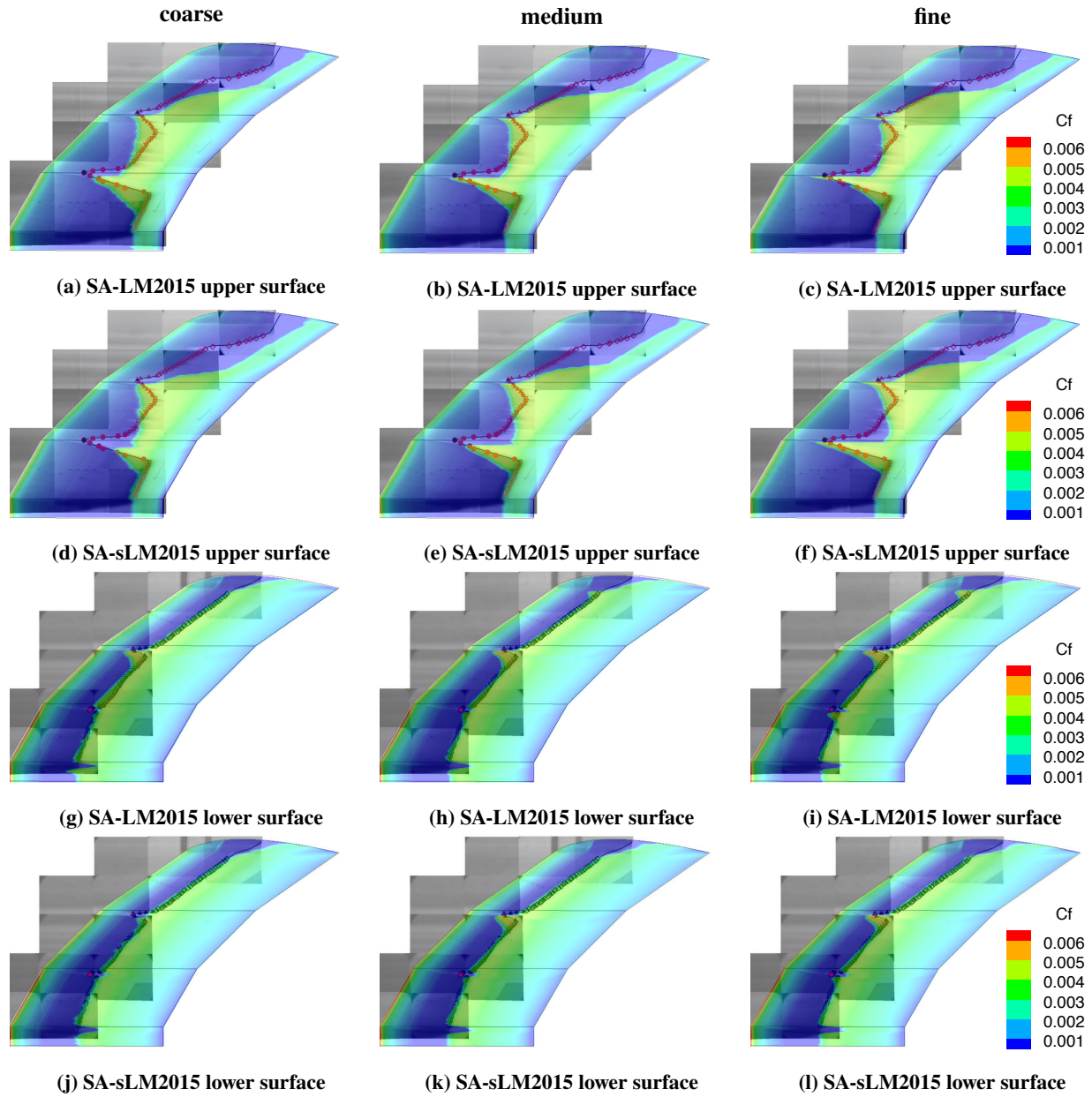
Fig. 12 Skin friction profiles on the upper and lower surfaces of the Sickle Wing for all grid levels overlaid with experimental transition locations [89]. Results were obtained using the SA-LM2015 and SA-sLM2015 transition models at $M = 0.16$, $\alpha = -2.6°$, $Tu = 0.17\%$, $h = 9.78\mu$m, and a Reynolds number of 2.75×10^6.

slightly downstream and agrees well with experiment. The transition front on the upper surface, where crossflow-induced transition is the primary mechanism, appears more sensitive to the grid refinement. The transition locations at the kink regions move upstream as the stationary crossflow vortices are better resolved. The lift and drag grid convergence for both models is presented in Figure 13(b).

The pressure coefficient profiles are extracted at the midspan of each sweep section for the fine grid, corresponding to spanwise sections at 25%, 55%, and 85% span, and are compared with the experimental profiles presented by Kruse
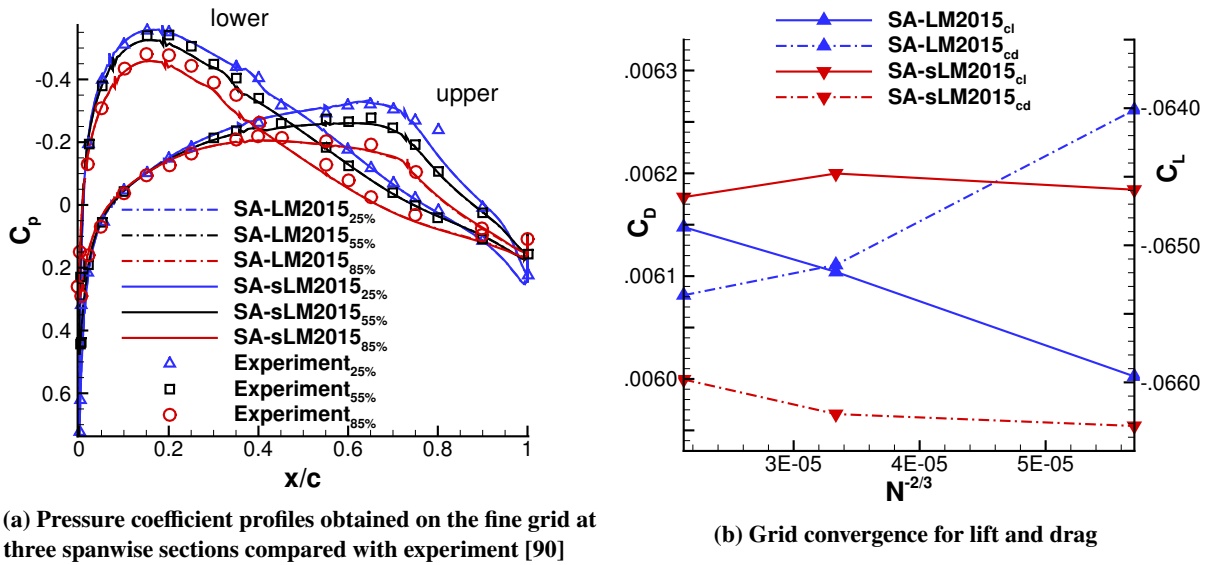
(a) Pressure coefficient profiles obtained on the fine grid at three spanwise sections compared with experiment [90]

(b) Grid convergence for lift and drag

Fig. 13 **Experimental and fine grid pressure coefficient profiles, and grid convergence for the SA-LM2015 and SA-sLM2015 transition models. The Sickle Wing was simulated at** $M = 0.16$**,** $\alpha = -2.6°$**,** $Tu = 0.17\%$**, and a Reynolds number of** 2.75×10^6 **[90].**

et al. [90] in Figure 13(a). The pressure coefficient profiles from the simulations lie on top of one another and the results demonstrate the 'wiggles' observed in experiment at approximately x/c = 0.35, corresponding to natural-transition on the lower surface of the Sickle Wing, are accurately reproduced[90]. There is a slight deviation between the simulations and experiment at 25% span on the upper surface of the Sickle Wing where both transition models, SA-LM2015 and SA-sLM2015, predict crossflow-induced transition upstream of the transition location in the experiment, which is triggered at x/c = 0.80 by a laminar separation bubble [89, 90]. This deviation is also illustrated in Figures 12(a-f) and is consistent with results obtained using the LM2015 transition model [44].

The relative residual and drag coefficient convergence histories are presented in Figure 14. The flow complexity in this case slows convergence for both models, however the smooth-variant displays improved residual convergence behaviour in Figures 14(a-c). The drag convergence, the magnitude of the difference between the current drag coefficient and the converged drag coefficient, plotted in Figures 14(d-f) show that the SA-sLM2015 model leads to faster convergence of the drag coefficient.

VI. Conclusions and Future Work

A novel coupling of the γ-$\tilde{R}e_{\theta t}$ LM2015 transition model with helicity-based crossflow correlations [43] and the one-equation SA turbulence model has been developed and designated SA-LM2015. The modifications maintain the fully local formulation pioneered by Langtry and Menter [29]. Smooth approximations to non-differentiable and stiff functions in the SA-LM2015 model are introduced in order to eliminate discontinuities and improve numerical behaviour,
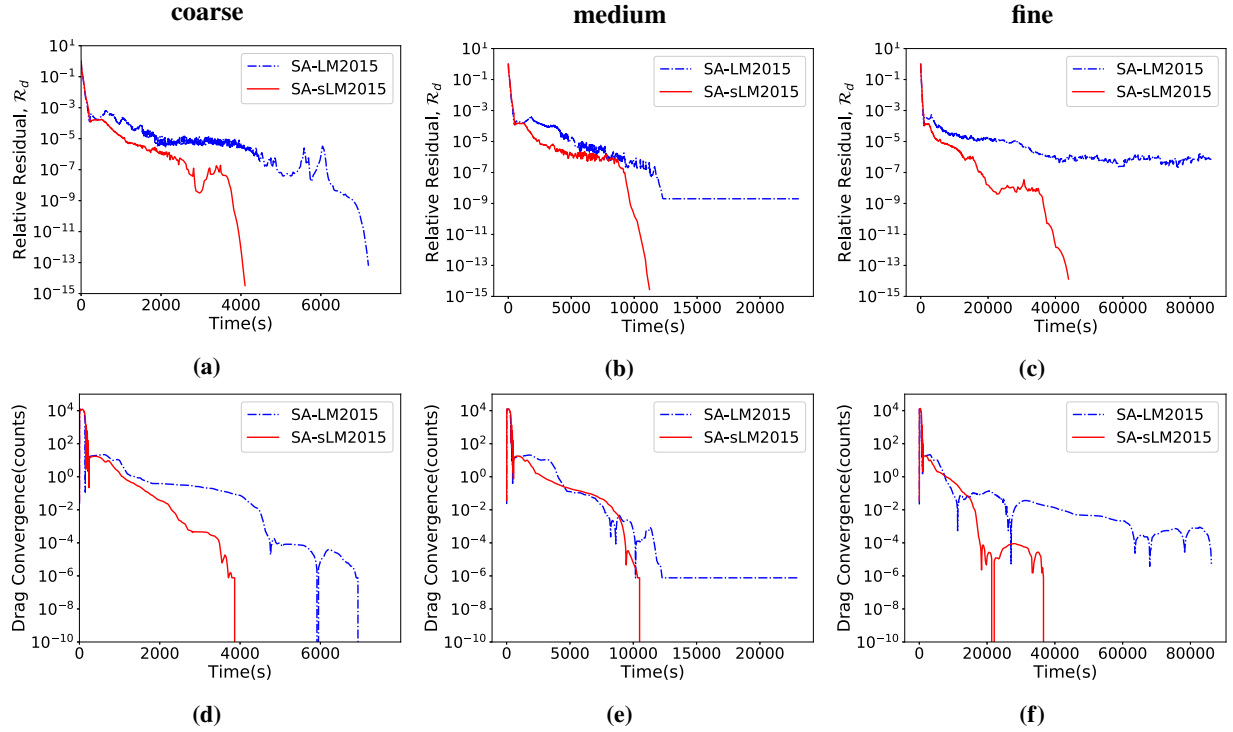
Fig. 14 Relative residual and drag coefficient convergence histories for the SA-LM2015 and SA-sLM2015 transition models on all grid levels, with the grids split into 592 computational blocks. The Sickle Wing was simulated at $M = 0.16$, $\alpha = -2.6°$, $Tu = 0.17\%$, $h = 9.78\mu$m, and a Reynolds number of 2.75×10^6.

with the smooth model designated SA-sLM2015. Deep convergence is achieved through the use of a fully-coupled, fully-implicit Newton-Krylov algorithm with modifications to the solution algorithm, including a source-term time stepping strategy, introduced to address the large source terms in the turbulence and transition model equations. Several of the strategies presented, including the smoothing techniques and source term time stepping, could be useful in the context of other transition models, specifically transition models which use similar intermittency transport equations, such as the following [35, 39, 40, 48, 91].

Simulations of the S809 and NLF0416 natural-laminar-flow airfoil test cases demonstrate that both models, SA-LM2015 and SA-sLM2015, are able to predict natural and separation-induced transition accurately, with the SA-sLM2015 model displaying improved numerical behaviour. Specifically, the new smooth formulations improve convergence, and combined with the new source term formulation, including limiting vorticity magnitude, oscillations near laminar separation bubbles produced by the LM2015 and SA-LM2015 models are eliminated. Three-dimensional simulations of the NLF2-0415 infinite swept wing and Sickle Wing test cases demonstrate that the model is able to capture the effects of crossflow accurately.

The SA-LM2015 and SA-sLM2015 transition models are validated in the current work using popular transition test cases under subsonic conditions. Future work will involve applying both transition models, SA-LM2015 and SA-sLM2015, to transonic transition test cases in order to confirm that the trends produced in subsonic flow extend to

higher Mach numbers.

Acknowledgments

References

[1] Green, J. E., "Civil aviation and the environment: the next frontier for the aerodynamicist," *Aeronautical Journal*, Vol. 110, No. 1110, 2006, pp. 469–486. doi:https://doi.org/10.1017/S0001924000001378.

[2] Bushnell, D. M., "Overview of aircraft drag reduction technology," *AGARD Report 786 (Special Course on Skin Friction Drag Reduction)*, 1992.

[3] Malik, M. R., Crouch, J. D., Saric, W. S., Lin, J. C., and Whalen, E. A., "Application of Drag Reduction Techniques to Transport Aircraft," *Encyclopedia of Aerospace Engineering*, 2015. doi:https://doi.org/10.1002/9780470686652.eae1013.

[4] Crouch, J. D., "Boundary-Layer Transition Prediction for Laminar Flow Control," *45th AIAA Fluid Dynamics Conference*, AIAA Paper 2015-2472, Dallas, TX, 2015. doi:https://doi.org/10.2514/6.2015-2472.

[5] Campbell, R. L., and Lynde, M. N., "Natural Laminar Flow Design for Wings with Moderate Sweep," *34th AIAA Applied Aerodynamics Conference*, AIAA Paper 2016-4326, Washington D.C., 2016. doi:https://doi.org/10.2514/6.2016-4326.

[6] Lynde, M. N., Campbell, R. L., Rivers, M. B., Viken, S. A., Chan, D. T., Watkins, N. A., and Goodliff, S. L., "Preliminary Results from an Experimental Assessment of a Natural Laminar Flow Design Method," *2019 AIAA Aerospace Sciences Meeting*, AIAA Paper 2019-2298, 2019. doi:https://doi.org/10.2514/6.2019-2298.

[7] Lynde, M. N., Campbell, R. L., and Viken, S. A., "Additional Findings from the Common Research Model Natural Laminar Flow Wind Tunnel Test," *AIAA Aviation 2019 Forum*, AIAA Paper 2019-3292, 2019. doi:https://doi.org/10.2514/6.2019-3292.

[8] Kenway, G. K. W., and Martins, J. R. R. A., "Multipoint High-Fidelity Aerostructural Optimization of a Transport Aircraft Configuration," *Journal of Aircraft*, Vol. 51, No. 1, 2014, pp. 144–160. doi:https://doi.org/10.2514/1.C032150.

[9] Reist, T. A., and Zingg, D. W., "High-Fidelity Aerodynamic Shape Optimization of a Lifting-Fuselage Concept for Regional Aircraft," *Journal of Aircraft*, Vol. 54, No. 3, 2016, pp. 1085–1097. doi:https://doi.org/10.2514/1.C033798.

[10] Reist, T. A., Zingg, D. W., Rakowitz, M., Potter, G., and Banerjee, S., "Multifidelity Optimization of Hybrid Wing-Body Aircraft with Stability and Control Requirements," *Journal of Aircraft*, Vol. 56, No. 2, 2018, pp. 442–456. doi:https://doi.org/10.2514/1.C034703.

[11] Reed, H. L., and Saric, W. S., "Transition mechanisms for transport aircraft," *38th Fluid Dynamics Conference and Exhibit*, AIAA Paper 2008-3743, Seattle, Washington, 2008. doi:https://doi.org/10.2514/6.2008-3743.

[12] Arnal, D., Casalis, G., and Houdeville, R., "Practical Transition Prediction Methods: Subsonic and Transonic Flows," *VKI*

Lecture Series: Advances in Laminar-Turbulent Transition Modeling, 2009.

[13] Aupoix, B., Arnal, D., Bezard, H., Chaouat, B., and Chedevergne, F., "Transition and Turbulence Modeling," *AerospaceLab*, 2011, pp. 1–13.

[14] Pasquale, D., Rona, A., and Garrett, S. J., "A selective review of CFD transition models," *39th AIAA Fluid Dynamics Conference*, AIAA Paper 2009-3812, San Antonio, Texas, 2009. doi:https://doi.org/10.2514/6.2009-3812.

[15] Savill, A. M., "By-pass transition using conventional closures," *Closure strategies for turbulent and transitional flows, Cambridge University Press, Cambridge*, Vol. 17, 2002, pp. 464–492. doi:https://doi.org/10.1017/CBO9780511755385.019.

[16] Halila, G. L. O., Chen, G., Shi, Y., Fidkowksi, K., Martins, J. R. R. A., and Mendonca, M. T., "High-Reynolds number transitional flow simulation via parabolized stability equations with an adaptive RANS solver," *Aerospace Science and Technology*, Vol. 91, 2019, pp. 321–336. doi:https://doi.org/10.1016/j.ast.2019.05.018.

[17] Drela, M., and Giles, M. B., "Viscous-inviscid analysis of transonic and low Reynolds number airfoils," *AIAA Journal*, Vol. 25, No. 10, 1987, pp. 1347–1355. doi:https://doi.org/10.2514/3.9789.

[18] Rashad, R., and Zingg, D. W., "Aerodynamic shape optimization for natural laminar flow using a discrete-adjoint approach," *AIAA Journal*, Vol. 54, No. 11, 2016, pp. 3321–3337. doi:https://doi.org/10.2514/1.J054940.

[19] Mayda, E., "Boundary Layer Transition Prediction for Reynolds-Averaged Navier-Stokes Methods," Ph.D. thesis, University of California, Davis, 2007.

[20] Stock, H. W., "e^N Transition Prediction in Three-Dimensional Boundary Layers on Inclined Prolate Spheroids," *AIAA Journal*, Vol. 44, No. 1, 2006, pp. 108–118. doi:https://doi.org/10.2514/1.16026.

[21] Krimmelbein, N., and Radespiel, R., "Transition prediction for three-dimensional flows using parallel computation," *Computers and Fluids*, Vol. 38, No. 1, 2009, pp. 121–136. doi:https://doi.org/10.1016/j.compfluid.2008.01.004.

[22] Arnal, D., Habiballah, M., and Coutols, E., "Laminar instability theory and transition criteria in two and three-dimensional flow," *La Recherche Aérospatiale*, , No. 2, 1984, pp. 125–143.

[23] Krumbein, A., Krimmelbein, N., and Schrauf, G., "Automatic transition prediction in hybrid flow solver, part 1: Methodology and sensitivities," *Journal of Aircraft*, Vol. 46, No. 4, 2009, pp. 1176–1190. doi:https://doi.org/10.2514/1.39736.

[24] Krumbein, A., Krimmelbein, N., and Schrauf, G., "Automatic transition prediction in hybrid flow solver, part 2: Practical application," *Journal of Aircraft*, Vol. 46, No. 4, 2009, pp. 1191–1199. doi:https://doi.org/10.2514/1.39738.

[25] Moens, F., Perraud, J., Krumbein, A., Toulorge, T., Iannelli, P., and Hanifi, A., "Transition prediction and impact on a three-dimensional high-lift-wing configuration," *Journal of Aircraft*, Vol. 45, No. 5, 2008, pp. 1751–1766. doi:https://doi.org/10.2514/1.36238.

[26] Streit, T., Horstmann, H., Shraut, G., Hein, S., Fey, U., Egmai, Y., Perraud, J., Salah El Din, I., Cella, U., and Quest, J., "Complementary numerical and experimental data analysis of the ETW Telfona Pathfinder wing transition tests," *49th Aerospace Sciences Meeting and Exhibit*, AIAA Paper 2011-881, Orlando, Florida, January, 2011. doi:https://doi.org/10.2514/6.2011-881.

[27] Shi, Y., Gross, R., Mader, C. A., and Martins, J., "Transition Prediction Based on Linear Stability Theory with the RANS Solver for Three-Dimensional Configurations," *2018 AIAA Aerospace Sciences Meeting*, AIAA Paper 2018-0819, 2018. doi:https://doi.org/10.2514/6.2018-0819.

[28] Seyfert, C., and Krumbein, A., "Evaluation of a Correlation-Based Transition Model and Comparison with the e^N Method," *Journal of Aircraft*, Vol. 49, No. 6, 2012, pp. 1765–1773. doi:https://doi.org/10.2514/1.C031448.

[29] Langtry, R. B., and Menter, F. R., "Correlation-based transition modeling for unstructured parallelized computational fluid dynamics codes," *AIAA Journal*, Vol. 47, No. 12, 2009, pp. 2894–2906. doi:https://doi.org/10.2514/1.42362.

[30] Coder, J. G., and Maughmer, M. D., "A CFD-Compatible Transition Model using an Amplification Factor Transport Equation," *51st AIAA Aerospace Sciences Meeting including the New Horizons Forum and Aerospace Exposition*, AIAA Paper 2013-0253, 2013. doi:https://doi.org/10.2514/6.2013-253.

[31] Coder, J. G., and Maughmer, M. D., "Computational fluid dynamics compatible transition modeling using an amplification factor transport equation," *AIAA Journal*, Vol. 52, No. 11, 2014, pp. 2506–2512. doi:https://doi.org/10.2514/1.J052905.

[32] Coder, J. G., "Enhancement of the Amplification Factor Transport Transition Modeling Framework," *55th AIAA Aerospace Sciences Meeting*, AIAA Paper 2017-1709, 2017. doi:https://doi.org/10.2514/6.2017-1709.

[33] Stefanski, D., Glasby, R., Erwin, J. T., and Coder, J. G., "Development of a Predictive Capability for Laminar-Turbulent Transition in HPCMP CREATETM-AV Kestrel Component COFFE using the Amplification Factor Transport Model," *2018 AIAA Aerospace Sciences Meeting*, AIAA Paper 2018-1041, 2018. doi:https://doi.org/10.2514/6.2018-1041.

[34] Coder, J. G., Pulliam, T. H., and Jensen, J. C., "Contributions to HiLiftPW-3 Using Structured, Overset Grid Methods," *2018 AIAA Aerospace Sciences Meeting*, AIAA Paper 2018-1039, 2018. doi:https://doi.org/10.2514/6.2018-1039.

[35] Coder, J. G., "Further Development of the Amplification Factor Transport Transition Model for Aerodynamic Flows," *2019 AIAA Aerospace Sciences Meeting*, AIAA Paper 2019-0039, 2019. doi:https://doi.org/10.2514/6.2019-0039.

[36] Spalart, P. R., and Allmaras, S. R., "A one equation turbulence model for aerodynamic flows," *30th AIAA Aerospace Sciences Meeting and Exhibit*, AIAA Paper 092-0439, Reno, Nevada, United States 1992. doi:https://doi.org/10.2514/6.1992-439.

[37] Xu, J., Han, X., Qiao, L., Bai, J., and Zhang, Y., "Fully Local Amplification Factor Transport Equation for Stationary Crossflow Instabilities," *AIAA Journal*, Vol. 57, No. 7, 2019, pp. 2682–2693. doi:https://doi.org/10.2514/1.J057502.

[38] Choi, J. H., and Kwon, O. J., "Enhancement of a Correlation-Based Transition Turbulence Model for Simulating Crossflow Instability," *AIAA Journal*, Vol. 53, No. 10, 2015, pp. 3063–3072. doi:https://doi.org/10.2514/1.J053887.

[39] Grabe, C., and Krumbein, A., "Correlation-Based Transition Modeling for Three-Dimensional Aerodynamic Configurations," *Journal of Aircraft*, Vol. 50, No. 5, 2013, pp. 1533–1539. doi:https://doi.org/10.2514/1.C032063.

[40] Grabe, C., Shengyang, N., and Krumbein, A., "Transition Transport Modeling for the Prediction of Crossflow Transition," *34th AIAA Applied Aerodynamics Conference*, AIAA Paper 2016-3572, Washington D.C., June, 2016. doi:https://doi.org/10.2514/6.2016-3572.

[41] Xu, J. K., Bai, J. Q., Qiao, L., and Zhang, Y., "Correlation-Based Transition Transport Modeling for Simulating Crossflow Instabilities," *Journal of Applied Fluid Mechanics*, Vol. 9, No. 5, 2016, pp. 2435–2442. doi:https://doi.org/10.18869/acadpub.jafm.68.236.25356.

[42] Muller, C., and Herbst, F., "Modelling of Crossflow-Induced Transition Based on Local Variables," *6th European Conference on Computational Fluid Dynamics (ECFD)*, 2014.

[43] Langtry, R. B., Sengupta, K., Yeh, D. T., and Dorgan, A. J., "Extending the γ-$\tilde{Re}_{\theta t}$ Correlation based Transition Model for

Crossflow Effects," *45th AIAA Fluid Dynamics Conference*, AIAA Paper 2015-2474, 2015. doi:https://doi.org/10.2514/6.2015-2474.

[44] Venkatachari, B. S., Paredes, P., Derlaga, J. M., Buning, P., Choudhari, M., Li, F., and Chang, C. L., "Assessment of Transition Modeling Capability in OVERFLOW with Emphasis on Swept-Wing Configurations," *2020 AIAA Aerospace Sciences Meeting*, AIAA Paper 2020-1034, 2020. doi:https://doi.org/10.2514/6.2020-1034.

[45] Menter, F. R., "Two-Equation Eddy-Viscosity Turbulence Models for Engineering Applications," *AIAA Journal*, Vol. 32, No. 8, 1994, pp. 1598–1605. doi:https://doi.org/10.2514/3.12149.

[46] Nie, S., Krimmelbein, N., Krumbein, A., and Grabe, C., "Extension of a Reynolds-stress-based Transition Transport Model for Crossflow Transition," *Journal of Aircraft*, Vol. 55, No. 4, 2018, pp. 1641–1654. doi:https://doi.org/10.2514/1.C034586.

[47] Medida, S., and Baeder, J. D., "Application of the Correlation-based γ-$\tilde{Re}_{\theta t}$ Transition Model to the Spalart-Allmaras Turbulence Model," *20th AIAA Computational Fluid Dynamics Conference*, AIAA Paper 2011-3979, Honolulu, HI, 2011. doi:https://doi.org/10.2514/6.2011-3979.

[48] Jung, Y. S., and Baeder, J. D., "γ-$\tilde{Re}_{\theta t}$-SA with Crossflow Transition Model using Hamiltonian-Strand Approach," *2018 AIAA Aerospace Sciences Meeting*, AIAA Paper 2018-1040, 2018. doi:https://doi.org/10.2514/6.2018-1040.

[49] Carnes, J. A., and Coder, J. G., "Effect of Crossflow on the S-76 and PSP Rotors in Hover," *2020 AIAA Aerospace Sciences Meeting*, AIAA Paper 2020-0773, 2020. doi:https://doi.org/10.2514/6.2020-0773.

[50] Schucker, J., "Development of a Three-Equation γ-$\tilde{Re}_{\theta t}$-Spalart-Allmaras Turbulence-Transition Model," Master's thesis, DLR, 2012.

[51] Langtry, R. B., "A correlation-based transition model using local variables for unstructured parallelized CFD codes," Ph.D. thesis, DLR, 2006.

[52] Pulliam, T. H., and Zingg, D. W., *Fundamental algorithms in computational fluid dynamics*, Springer International Publishing, 2014.

[53] Suluksna, K., Dechaumphai, P., and Juntasaro, E., "Correlations for modeling transitional boundary layers under influences of freestream turbulence and pressure gradient," *International Journal of Heat and Fluid Flow*, Vol. 30, No. 1, 2009, pp. 66–75. doi:https://doi.org/10.1016/j.ijheatfluidflow.2008.09.004.

[54] Allmaras, S. R., and Johnson, F. T., "Modifications and clarifications for the implementation of the Spalart-Allmaras turbulence model," *Seventh International Conference on Computational Fluid Dynamics*, ICCFD7 Paper 1902, 2012, pp. 1–11.

[55] Osusky, M., "A Parallel Newton-Krylov-Schur Algorithm for the Reynolds-Averaged Navier-Stokes Equations," Ph.D. thesis, Graduate Department of Aerospace Science and Engineering, University of Toronto, 2013.

[56] Bertsekas, D. P., "Nondifferentiable optimization via approximation," *Mathematical Programming Study 3*, 1975, pp. 1–25. doi:https://doi.org/10.1007/BFb0120696.

[57] Chakraborty, A., Sinha Roy, A., and Dasgupta, B., "Non-parametric Smoothing for Gradient Methods in Non-differentiable Optimization Problems," *2016 IEEE International Conference on Systems, Man, and Cybernetics*, 2016. doi:https://doi.org/10.1109/SMC.2016.7844819.

[58] Rivest, R. L., "Game Tree Searching by Min/Max Approximation," *Artificial Intelligence*, Vol. 34, No. 1, 1988, pp. 77–96.

doi:https://doi.org/10.1016/0004-3702(87)90004-X.

[59] Pee, E. Y., "On Solving Large-Scale Finite Minimax Problems using Exponential Smoothing," *Journal of Optimization Theory and Applications*, Vol. 148, No. 2, 2011, pp. 390–421. doi:https://doi.org/10.1007/s10957-010-9759-1.

[60] Polak, E., Royset, J. O., and Womersley, R. S., "Algorithms with Adaptive Smoothing for Finite Mini-max Problems," *Journal of Optimization Theory and Applications*, Vol. 119, No. 3, 2003, pp. 459–484. doi:https://doi.org/10.1023/B:JOTA.0000006685.60019.3e.

[61] Li, X., "An Entropy-Based Aggregate Method for Minimax Optimization," *Engineering Optimization*, Vol. 18, No. 4, 1997, pp. 277–285. doi:https://doi.org/10.1080/03052159208941026.

[62] Rashad, R., "High-Fidelity Aerodynamic Shape Optimization for Natural Laminar Flow," Ph.D. thesis, University of Toronto, 2016.

[63] Richards, F. J., "A Flexible Growth Function for Empirical Use," *Journal of Experimental Botany*, Vol. 10, No. 2, 1959, pp. 290–301. doi:https://doi.org/10.1093/jxb/10.2.290.

[64] Hicken, J. E., and Zingg, D. W., "Parallel Newton-Krylov solver for the Euler equations discretized using simultaneous approximation terms," *AIAA Journal*, Vol. 46, No. 11, 2008, pp. 2773–2786. doi:https://doi.org/10.2514/1.34810.

[65] Osusky, M., and Zingg, D. W., "Parallel Newton-Krylov-Schur Flow Solver for the Navier-Stokes Equations," *AIAA Journal*, Vol. 51, No. 12, 2013, pp. 2833–2851. doi:https://doi.org/10.2514/1.J052487.

[66] Saad, Y., and Schultz, M. H., "GMRES: A generalized minimal residual algorithm for solving nonsymmetric linear systems," *SIAM Journal on Scientific and Statistical Computing*, Vol. 7, No. 3, 1986, pp. 856–869. doi:https://doi.org/10.1137/0907058.

[67] Saad, Y., and Sosonkina, M., "Distributed Schur complement techniques for general sparse linear systems," *SIAM Journal of Scientific Computing*, Vol. 21, 1999, pp. 1337–1357. doi:https://doi.org/10.1137/S1064827597328996.

[68] Moryossef, Y., and Levy, Y., "Unconditionally positive implicit procedure for two-equation turbulence models: Application to k-ω turbulence models," *Journal of Computational Physics*, Vol. 220, 2006, pp. 88–108. doi:https://doi.org/10.1016/j.jcp.2006.05.001.

[69] Lian, C., Xia, G., and Merkle, C. L., "Impact of source terms on reliability of CFD algorithms," *Computers & Fluids*, Vol. 39, 2010, pp. 1909–1922. doi:https://doi.org/10.1016/j.compfluid.2010.06.021.

[70] Moryossef, Y., and Levy, Y., "The unconditionally positive-convergent implicit time integration scheme for two-equation turbulence models: Revisited," *Computers & Fluids*, Vol. 38, 2009, pp. 1984–1994. doi:https://doi.org/10.1016/j.compfluid.2009.06.005.

[71] Moryossef, Y., "Unconditionally stable time marching scheme for Reynolds stress models," *Journal of Computational Physics*, Vol. 276, 2014, pp. 635–664. doi:https://doi.org/10.1016/j.jcp.2014.07.047.

[72] Mosahebi, A., and Laurendeau, E., "Convergence Characteristics of Fully and Loosely Coupled Numerical Approaches for Transition Models," *AIAA Journal*, Vol. 53, No. 5, 2015, pp. 1399–1404. doi:https://doi.org/10.2514/1.J053722.

[73] Mosahebi, A., and Laurendeau, E., "Introduction of a modified segregated numerical approach for efficient simulation of γ-$\tilde{Re}_{\theta t}$ transition model," *International Journal of Computational Fluid Dynamics*, Vol. 29, 2015, pp. 357–375. doi:https://doi.org/10.1080/10618562.2015.1093624.

[74] Candler, G. V., Subbareddy, P. K., and Nompelis, I., "Decoupled Implicit Method for Aerothermodynamics and Reacting Flows," *AIAA Journal*, Vol. 51, No. 5, 2013, pp. 1245–1254. doi:https://doi.org/10.2514/1.J052070.

[75] Chisholm, T. T., and Zingg, D. W., "A Jacobian-free Newton-Krylov algorithm for compressible turbulent fluid flows," *Journal of Computational Physics*, Vol. 228, No. 9, 2009, pp. 3490–3507. doi:https://doi.org/10.1016/j.jcp.2009.02.004.

[76] Yildirim, A., Kenway, G. K. W., Mader, C. A., and Martins, J. R. R. A., "A Jacobian-free approximate Newton-Krylov startup strategy for RANS simulations," *Journal of Computational Physics*, 2019. doi:https://doi.org/10.1016/j.jcp.2019.06.018.

[77] Lian, C., Xia, G., and Merkle, C. L., "Solution-limited time stepping to enhance reliability in CFD applications," *Journal of Computational Physics*, Vol. 228, 2009, pp. 4836–4857. doi:https://doi.org/10.1016/j.jcp.2009.03.040.

[78] Modisette, J. M., "An automated reliable method for two-dimensional Reynolds-Averaged Navier-Stokes simulations," Ph.D. thesis, Massachusetts Institute of Technology, 2011.

[79] Swanson, R. C., and Turkel, E., "On central-difference and upwind schemes," *Journal of Computational Physics*, Vol. 101, 1992, pp. 292–306. doi:https://doi.org/10.1016/0021-9991(92)90007-L.

[80] Somers, D. M., "Design and experimental results for a natural-laminar-flow airfoil for general aviation applications," *NASA TP-1861*, 1981.

[81] Coder, J. G., "Standard Test Cases for Transition Model Verification and Validation in Computational Fluid Dynamics," *2018 AIAA Aerospace Sciences Meeting*, AIAA Paper 2018-0029, 2018. doi:https://doi.org/10.2514/6.2018-0029.

[82] Denison, M., and Pulliam, T. H., "Implementation and Assessment of the Amplification Factor Transport Laminar-Turbulent Transition Model," *2018 AIAA Aerospace Sciences Meeting*, AIAA Paper 2018-3382, 2018. doi:https://doi.org/10.2514/6.2018-3382.

[83] Khayatzadeh, P., and Nadarajah, S. K., "Laminar-Turbulent Flow Simulation for Wind Turbine Profiles using the γ-$\tilde{Re}_{\theta t}$ Transition Model," *Wind Energy*, Vol. 17, No. 6, 2014, pp. 901–918. doi:https://doi.org/10.1002/we.1606.

[84] Somers, D. M., "Design and experimental results for the S809 airfoil," *National Renewable Energy Laboratory, Golden, Colorado*, NRELSR-440-6918, 1989. doi:https://doi.org/10.2172/437668.

[85] Dagenhart, J., and Saric, W., "Crossflow stability and transition experiments in swept-wing flow," *NASA Langley Technical Report Server*, Vol. NASA/TP-1999-209344, 1999.

[86] Radeztsky, R. H., Reibert, M. S., and Saric, W. S., "Effect of Micron-Sized Roughness on Transition in Swept-Wing Flows," *31st Aerospace Sciences Meeting and Exhibit*, AIAA Paper 93-0076, 1993. doi:https://doi.org/10.2514/6.1993-76.

[87] Jameson, A., Schmidt, W., and Turkel, E., "Numerical solution of the Euler equations by finite volume methods using Runge-Kutta time-stepping schemes," *14th Fluid and Plasma Dynamics Conference*, AIAA Paper 81-1259, 1981. doi:https://doi.org/10.2514/6.1981-1259.

[88] Pulliam, T. H., "Efficient solution methods for the Navier-Stokes equations," *Tech. rep., Lecture Notes for the von Karman Inst. for Fluid Dynamics Lecture Series: Numerical Techniques for Viscous Flow Computation in Turbomachinery Bladings*, 1986.

[89] Petzold, R., and Radespiel, R., "Transition on a Wing with Spanwise Varying Crossflow and Linear Stability Analysis," *AIAA Journal*, Vol. 53, No. 2, 2015, pp. 321–335. doi:https://doi.org/10.2514/1.J053127.

[90] Kruse, M., Munoz, F., and Radespiel, R., "Transition Prediction Results for Sickle Wing and NLF(1)-0416 Test Cases," *2018*

AIAA Aerospace Sciences Meeting, AIAA Paper 2018-0537, 2018. doi:https://doi.org/10.2514/6.2018-0537.

[91] Menter, F. R., Smirnov, P. E., Liu, T., and Avancha, R., "A One-Equation Local Correlation-Based Transition Model," *Flow, Turbulence and Combustion*, Vol. 95, 2015, pp. 583–619. doi:https://doi.org/10.1007/s10494-015-9622-4.